ADVANCED MATERIALS
www.advmat.de

Engineering Grain Boundaries in Two-Dimensional Electronic Materials

*Seong-Jun Yang, Min-Yeong Choi, and Cheol-Joo Kim**

Engineering the boundary structures in 2D materials provides an unprecedented opportunity to program the physical properties of the materials with extensive tunability and realize innovative devices with advanced functionalities. However, structural engineering technology is still in its infancy, and creating artificial boundary structures with high reproducibility remains difficult. In this review, various emergent properties of 2D materials with different grain boundaries, and the current techniques to control the structures, are introduced. The remaining challenges for scalable and reproducible structure control and the outlook on the future directions of the related techniques are also discussed.

1. Introduction

The 2D materials are low-dimensional electronic components for fabricating next-generation device architectures from thin-film circuitry with advanced functionalities to novel quantum devices.[1–3] Key advantages of the materials originate from the anisotropic 2D structures. From a technical viewpoint, state-of-the-art device fabrication techniques, including the key processes for growth, patterning, and metallization have been developed for planar structures; therefore, the techniques can be readily applied to engineer the materials. After the device fabrications, the electrons are strongly confined into the atomically thin geometry toward the out-of-plane direction, resulting in desirable characteristics by strong confinement effects, such as reduced leakage current and enhanced photoluminescence quantum yield.[4,5] However, electrons are delocalized along the in-plane direction, enabling efficient electrical manipulation and detection of the confined electronic states with high conductivities and bandwidths.[6] As the 2D materials have self-passivating nature with dangling-bond-free surfaces, they can maintain their intrinsic properties even in the ultrathin structures and can be integrated with preexisting electronic components by forming pristine interfaces.[7–9]

S.-J. Yang, M.-Y. Choi, C.-J. Kim
Center for Epitaxial van der Waals Quantum Solids
Institute for Basic Science (IBS)
Pohang, Gyeongbuk 37673, Republic of Korea
E-mail: kimcj@postech.ac.kr
S.-J. Yang, M.-Y. Choi, C.-J. Kim
Department of Chemical Engineering
Pohang University of Science and Technology
Pohang, Gyeongbuk 37673, Republic of Korea
The ORCID identification number(s) for the author(s) of this article can be found under https://doi.org/10.1002/adma.202203425.

DOI: 10.1002/adma.202203425

To utilize the intrinsic properties of 2D materials, it is important to control both interlayer interfaces and intralayer dislocations. Significant efforts have been made mostly to suppress the formation of crystalline disorders by developing advanced material growths[10–12] and integration techniques,[13] resulting in single-crystalline materials with atomically clean interfaces. However, structural boundaries can provide exciting control knobs to program the material properties beyond what is available in the thermodynamically most stable forms if the boundaries are fabricated controllably. Prototypical examples are the electrical doping of materials by introducing impurities[14] and optimizing device performances for targeted functionalities by forming heterojunctions.[15] Furthermore, 2D materials of van der Waals (vdW) structures arbitrarily enable the control of their atomic configurations due to the weak interlayer interactions. Therefore, various types of structural boundaries with different crystalline symmetries and band structures have been reported even in a single material platform by atomic displacements,[16,17] crystalline misorientation,[18] and distortions of chemical bonding[19,20] without the introduction of foreign materials. They have provided testbeds to discover novel electrical properties,[21] which are inaccessible in perfect crystals. However, direct applications of the material properties are elusive due to the lack of techniques to precisely control the boundaries over technologically relevant scales.

In this review, we discuss about the emerging properties of structural boundaries in vdW structures and the developments of techniques to control the boundaries at the atomic scale. We focus on boundary structures caused by atomic displacements within a single-crystalline material, rather than heterogeneous boundaries with chemical complexity, which have been summarized in detail elsewhere.[22] We discuss the remaining critical issues to reproduce functional boundaries by a designer approach for the discovery of properties and applications in electronics and provide our outlook on the directions in the field.

2. Boundary Types and Related Properties in vdW Solids

A grain boundary is an interfacial plane that exists between two perfect crystallites. The boundaries are not randomly formed, and the resultant structures are restricted by the crystalline lattices, in which they are embedded. The structural defects emerge at the boundaries of misaligned crystalline domains, whose rotation axis most likely points to the out-of-plane

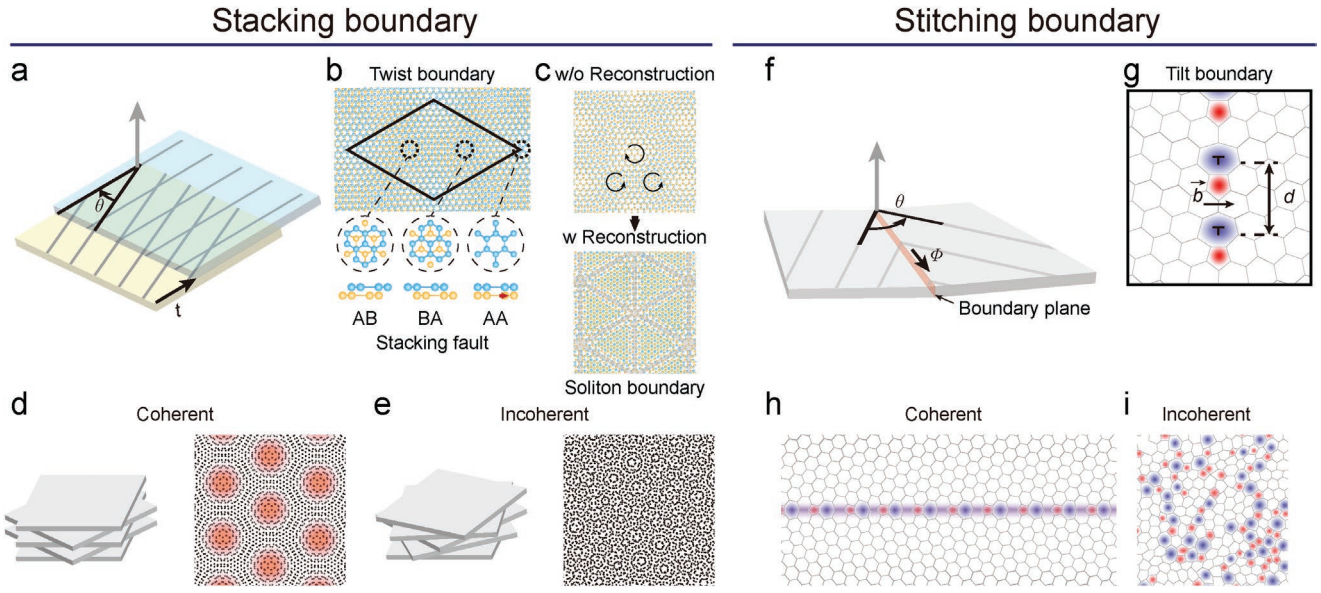

Figure 1. Boundaries in 2D materials. a) Schematic of stacking boundary. Two structure parameters, the relative interlayer rotation angle, θ, and the relative translation of domains, t, determine the boundary structure. b) Schematics of the atomic structure of twist boundary (top) with local stacking faults (bottom). Twist boundary is formed by rotating two lattices, making different local stacking orders. The stacking fault is formed when a single plane is translated laterally with respect to the other plane. c) Schematics of twisted bilayer structures without (w/o) (top) and with (w) (bottom) atomic reconstruction. Soliton boundary (gray dashed area) is formed by atomic reconstruction between crystalline domains (green area). Schematics of crystal structures with d) coherent and e) incoherent stacking boundaries. Coherent stacking boundary forms periodic moiré patterns through the interfaces. f) Schematic of stitching boundary. The structure of the tilt boundary is determined by the tilt angle, θ, and the stitching orientation, Φ. g) Schematic of the atomic structure of tilt boundary formed in merged hexagonal lattices. 5|7 defects (red and blue dots) are periodically separated by d with Burgers vector $\vec{b}$. Schematics of the atomic structure of h) coherent and i) incoherent stitching boundaries.

directions in vdW solids (**Figure 1**) due to the weak interlayer interactions. The misaligned domains can be either vertically stacked toward the rotation axis to form stacking boundaries (Figure 1a–e) or laterally stitched, perpendicular to the rotation axis to form stitching boundaries (Figure 1f–i). The space group, density, and arrangement of defects in each interface are determined by the structural parameters associated with the displacements of constituent domains in the host lattices.

The distorted chemical bonding in local defects results in electronic defect states distinct from that of perfect crystals. Collective electronic states with a structurally programmable density of states and band topology can emerge by the interaction between coherent defects in a periodic pattern at the interfaces (Figure 1d,h). Some of the symmetry elements of the perfect crystal can be broken in the individual defects and its lattice, emerging new properties (**Tables 1** and **2**) upon the external stimuli, which excites the electronic defect states. In addition, incoherent defects with a random arrangement can strongly disturb the intrinsic properties (Figure 1e,i), such as electrical and thermal conductivities of bulk crystals, depending on their density, and the resultant properties can be beneficial for certain applications.[23] Below, we discuss boundary-related structural and physical properties at both stacking and stitching boundaries of vdW materials.

Here, we note that there are many other grain boundaries, which cannot be classified as either stacking or stitching boundaries. For instance, the rotation axis for the misaligned domains can point to the in-plane direction, resulting in interfaces between edges and surfaces of 2D crystals.[24] While the boundaries with many dangling-bonds can provide useful properties such as enhanced catalytic reactions due to the high chemical reactivity, here we mainly focused on boundaries without dangling-bonds, where deterministic controls of the atomic structures are more feasible to precisely program the electrical properties.

2.1. Stacking Boundaries

For the formation of stacking boundaries, vdW interfaces are modulated by structural parameters of the relative interlayer rotation angle, θ, and the relative translation of domains, t (Figure 1a) between stacked domains. In the boundary with a finite θ and robust lattices, the interfacial plane between two crystalline domains is located at the interlayer boundary, resulting in moiré patterns (Figure 1b); the two crystalline domains are interfacing toward the out-of-plane direction. If structural reconstruction happens by interlayer interactions, intralayer boundaries (gray-colored regions in Figure 1c) are formed between crystalline multilayers (green-colored regions); the crystalline multilayer domains are interfacing toward the in-plane direction.[19] In both cases, networks of screw dislocations with a periodicity appear to modulate the electronic bands of the stacks by two key effects.

First, spatially varying local-stacking orders (Figure 1b) generate periodic potentials by interlayer interactions to modulate the electronic states of the same periodicity. With a broad tuning of $-180°/n < \theta < 180°/n$ for crystalline domains with an n-fold rotational symmetry, the bands are modulated at

Table 1. Summary of band features and emerging properties induced by stacking boundaries controlled by structural parameters.

Materials	Structures	Key band features	Key properties	Mechanisms	Refs.
Graphene	Rhombohedral ($t = a$)[a)]	Band gap	–	Dimerized sublattice hopping	[38]
	Twisted bilayer ($\theta = 1.06°$)	Flat bands	Superconductivity	Modulated interlayer coupling	[32]
	Twisted bilayer ($\theta = 1.6°$)	3/4filling insulating states	Ferromagnetism	Broken time-reversal symmetry	[33]
	Twisted bilayer ($\theta = 30°$)	Dirac cone replica	Quasicrystal	Modulated interlayer coupling	[148]
	Twisted bilayer ($\theta = 21.8°$)	Band gap	–	Broken sublattice symmetry	[149]
TMD	Rhombohedral ($\theta = 60°$)	–	Ferroelectricity	Broken out-of-plane polar symmetry	[150]
	Twisted bilayer ($\theta = 4.5°$)	Flat bands	Zero resistance	Modulated interlayer coupling	[151]
	Twisted bilayer (any θ)	Tunable van hove singularity	–	Modulated interlayer coupling	[30]
hBN	Rhombohedral ($\theta = 60°$)	–	Ferroelectricity	Broken out-of-plane polar symmetry	[48,49,152]
	Twisted bilayer (any θ)	Tunable van hove singularity	–	Modulated interlayer coupling	[153]
Chromium trihalide	Rhombohedral ($t = a$) *or* Twisted bilayer ($\theta = 180°$)	–	Ferromagnetism	Modulated interlayer coupling	[44–47]
All 2D	Any θ (achiral stack)[b)]	Out-of-plane dispersion	–	Modulated interlayer coupling	[154]
	Twisted multilayer (random θ)	–	Low out-of-plane thermal conductivity	Decoupled out-of-plane phonon transports	[23]

[a)]a: in-plane interatomic distance. [b)]Achiral stack is twisted multilayer films stacked with constant θ but alternating sign through all of interfaces.

θ-dependent energy levels and momentum spaces,[18,25] resulting in multiple new band extrema or valleys, with new band dispersions, gaps, and density of states (**Figure 2**a).[26] Depending on θ, optical absorptions and emissions between the interlayer states happen at different energy levels,[27–30] enabling optoelectronic properties in tunable spectral ranges. The electronic states at the emerging valleys have modulated Berry curvatures by quantum geometrical effects to guide the electrical currents, suggesting topological electronic devices.[31] In particular, flat bands with a low dispersion of electron kinetic energy can emerge, when the size of a supercell, a_m, becomes larger than the typical size of a unit cell for natural crystals, a, by several orders of magnitudes, following $a_m = a/\theta$ at the low θ regime. Because, the electron kinetic energy is proportional to $(1/a_m)^2$. The renormalized band structure host van Hove singularities with local density of states maxima, at which, Fermi level can be aligned to induce a conductance peak.[18] Interestingly, if the kinetic energy becomes smaller than the energy of electron-electron interactions between supercells, which is proportion to $1/a_m$, strongly correlated properties can emerge, including superconductivity,[32] magnetism, and Mott insulator.[33,34] More comprehensive discussions about the underlying mechanism for strongly correlated phenomena in the artificially stacked vdW crystals have been made in other literatures.[35–37]

In addition to θ, stacking faults by a finite t modulate the band structures. For example, multilayer graphene in particular stacking orders can have a profound effect on its electronic bands (Figure 2b,c). Multilayer graphene can have hexagonal and rhombohedral crystals with different stacking orders (Figure 2b). Contrary to energetically most stable hexagonal crystals, rhombohedral crystal host spontaneously gapped-bulk electronic states in ultrathin geometries (Figure 2c), attributed to the dimerized electronic states of opposite sublattices by interlayer hopping.[38,39] A new phase of a gapped quantum-spin Hall states with giant Berry curvature was observed, implying the application for novel phase-transition and topological devices. A different example is the stacks of layers with a trivial gap, such as hexagonal boron nitride (hBN). The size and type of band gap vary depending on the stacking orders;[40] therefore the efficiency of optoelectronic devices, such as light-emitting diodes and detectors can be modulated.[41] Other layered materials with different band topologies to extend the tunability for engineering the interlayer bands are present.[42,43]

Second, the underlying symmetry of the localized boundaries, distinct from that of natural crystals can induce new phenomena.

Table 2. Summary of band features and emerging properties of coherent stitching boundaries, as a function of dislocation structure caused by different structural parameters.

Materials	Structures[a)]	Key band features	Key properties	Mechanisms	Refs.
Graphene	5|7 cores ($\theta < 28°$, $\Phi = 0°$)	High dE/dK (low effective mass)	–		[17]
	Alternating[b)] 5|7 cores ($28° < \theta < 60°$, $\Phi = 30°$)	Band gap (≈1.04 eV)	Semiconducting properties	Broken symmetry	
	55|8, twin cores ($\theta = 0°$, $\Phi = 0°$)	High dE/dK (low effective mass)	1D metallic conductions	Inter-defect interactions	[73,155]
hBN	B 5|7[c)] and N 5|7 cores ($\theta < 32°$, $\Phi = 0°$ (60°))	Localized in-gap states Reduced band gaps	–	Homo-elemental bonds	[120,156]
	4|8 ($\theta < 32°$, $\Phi = 0°$)				
	Alternating 5|7 cores ($32° < \theta < 60°$, $\Phi \neq 0, 60°$)				
	Alternating 4|8 cores ($32° < \theta < 60°$, $\Phi \neq 0, 60°$)				
	55|8 or 6′6′ twin cores ($\theta = 60°$, $\Phi = 0$ or 60°)	Modulated band gaps (3.4 eV in 55|8 cores) (′0 eV in 6′6′ cores)	1D electrical conductions	Inter-defect interactions	[66]
TMD (MX_2)	M 5|7 derivatives (Mo 4|6, Mo 6|8 cores) ($\theta < 32°$, $\Phi = 0°$)	Mid-gap states Spin-polarized states Broaden band gaps	Ferromagnetism (M 5|7) Paramagnetism (Se-derivatives in WSe_2) Single-photon emission	Homo-elemental bonds Spin-spin interactions	[20,63,72,119,157,158]
	X 5|7 derivatives (S 4|6, S 6|8 cores) ($\theta < 32°$, $\Phi = 60°$)				
	Alternating 5|7 + hexagons cores ($32° < \theta < 47°$, $\Phi \neq 0, 60°$)		–		[63]
	Alternating 4|8 cores ($32° < \theta < 47°$, $\Phi \neq 0, 60°$)		–		[63]
	4|8 cores ($47° < \theta \leq 60°$, $\Phi \approx 0, 60°$)	Spin-polarized states	Antiferromagnetism	Spin-spin interactions	[63]
	Alternating M 5|7 + X 5|7 cores ($47° < \theta \leq 60°$, $\Phi \neq 0, 60°$)		–		[20]
	4|4 P, 4|4 E, 55|8 twin cores ($\theta = 60°$, $\Phi = 0, 60°$)	Quantized valence bands Modulated band gap Spin-polarized states	1D metallic wire Charge density wave Spin-, valley-polarized transport	Broken symmetry	[67–70,75,76,137,159]

[a)] $\Phi = 30°$ indicate zig–zag grain boundary, and $\Phi = 0°$ and 60° are arm-chair grain boundaries with different stitching directions[20,119]. [b)] Different defects are alternatively located along the boundary. [c)] M 5|7 means that the shared core of 5|7 defects is composed of M—M homoelemental bond.

There are several key symmetry elements such as inversion and chiral symmetries, which can be broken in stacking boundaries. When noncentrosymmetric monolayer of polar crystals with C_n rotational symmetries, such as hBN, transition metal dichalcogenides (TMDs), and CrX_3 (X = I, Cl, Br) with $n = 3$, are stacked into bilayers, the presence of inversion symmetry is determined by θ at the interface; the θ of $180°/n$ results in AA′ stacking configurations with inversion symmetry (Figure 2d), and the θ of 0° present AB stacking configurations with the broken inversion symmetry. The broken inversion symmetry in the AB stacks can result in different properties from the natural crystals with inversion symmetry. For instance, while CrX_3 crystals show antiferromagnetic ordering in the electron spins in the bulk forms, the magnetic ground states of multilayers with AB stacking orders host ferromagnetic orderings by changing the sign of interlayer exchange energy.[44–47] The stacking order is also associated with various other physical properties, including ferroelectricity (Figure 2e),[48,49] piezoelectricity,[50] pyroelectricity,[51] even-order

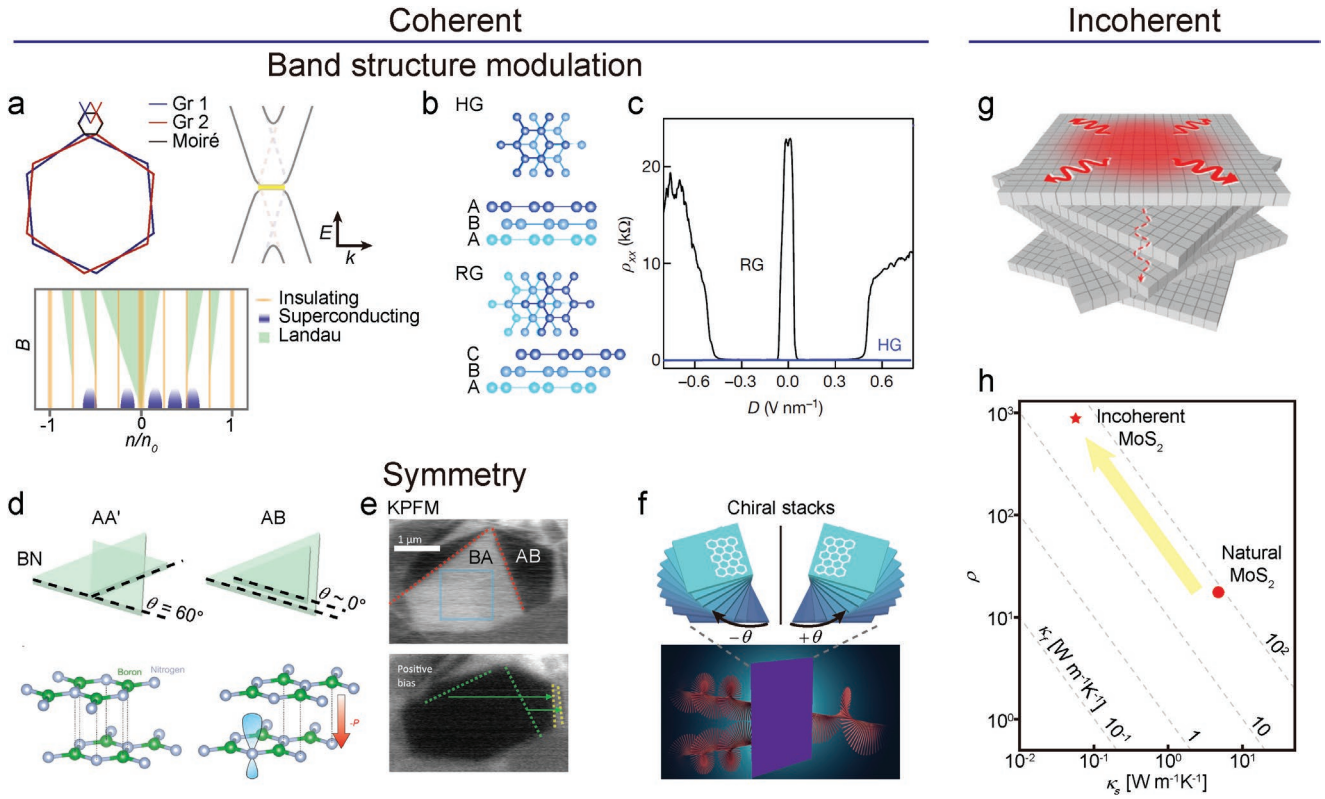

Figure 2. Stacking boundary-driven properties. a) Electronics structure of twisted bilayer graphene. Brillouin zone of twisted bilayer graphene and moiré Brillouin zone in k-space (top left) and electronic structure (top right). Interlayer hybridization produces flat bands at low energy in the case of the $\theta \approx 1.1°$. Landau fan diagram (bottom) of twisted bilayer graphene with highlighted electronic phases. b) Top and side view of hexagonal (HG, top) and rhombohedral (RG, bottom) graphite. c) Displacement field-dependent resistance of HG and RG. RG shows higher resistance than HG at zero and high displacement field, which indicates band gap opening. d) Schematics of twist angle-dependent two different stacking orders in 2D polar films, i.e. AA′ ($\theta = 60°$, left) and AB ($\theta = 0°$, right) stacked bilayer BN. Spontaneous polarization is induced by the distortion of the nitrogen $2p_z$ orbital in AB stacked bilayer BN. e) Polarization flipping measured by Kelvin probe force microscopy in AB stacked BN. f) Mirror symmetry in progressively twisted multilayer 2D films (top). The chirality of materials is determined by the rotational polarity of stacked layers ($\pm\theta$). Polarization direction-dependent interactions of circularly polarized light (bottom). g) Schematic of thermal anisotropy in 2D films with incoherent stacking boundaries. Thermal transport through out-of-plane shows that 1D glass-like thermal transport even that of in-plane direction is similar to bulk single crystals. h) Thermal anisotropy measured in coherently and incoherently stacked 2D crystals. In-plane (κ_j) and out-of-plane (κ_s) thermal conductivity are denoted by diagonal line (gray) and x axis. Incoherently stacked 2D crystal shows much higher thermal anisotropy than natural 2D crystal. c) Adapted with permission.[38] Copyright 2020, Springer Nature. d) Bottom: Adapted with permission.[48] Copyright 2021, American Association for the Advancement of Science. e) Adapted with permission.[49] Copyright 2021, American Association for the Advancement of Science. g) Adapted with permission.[23] Copyright 2021, Springer Nature.

nonlinear effect,[52,53] valley-contrasting properties,[54] and others,[55] which are absent in the energetically most stable AA′ stacks. The properties can be further enhanced by increasing the number of layers with the same θ, implying a route to enhance the targeted material properties.[49]

The twisted interfaces also can possess chiral symmetries with the absence of both mirror and inversion symmetries when the mirror planes of the stacked individual layers along the in-plane directions are not overlapped. Here, a chiral pair exists by twists with opposite rotational polarities ($\pm\theta$) (Figure 2f). One prototype-twisted multilayer, namely, a vertical superlattice with periodic structures along the vertical direction is sketched in Figure 2f. These twisted multilayers provide an opportunity to explore various structural chirality-dependent phenomena, including chiral orbital current,[56] circular dichroism,[57] and circular photogalvanic effect[58] with various stacking orders, which are periodic, aperiodic, and quasicrystals along the out-of-plane direction.

While we mostly discussed coherent electronic states from the periodic potentials across the interlayer interfaces, which naturally appear with a constant θ, incoherent states with amorphous-like features can be realized toward the out-of-plane direction, when θ for interfaces in multilayers are individually controlled to different values (Figure 2g). Out-of-plane electrical[59] and thermal conductivities[23] are suppressed, further enhancing the high anisotropy in the conductivity of layered structures (Figure 2h). They can be useful for thermal management[23] and low-k dielectric films.[60] In Table 1, we have listed examples of various stacking boundaries with different structural parameters and their properties.

2.2. Stitching Boundaries

Lateral stitching of tilted domains by θ form 1D lattice defects at the intralayer interfaces. The orientation of the stitching

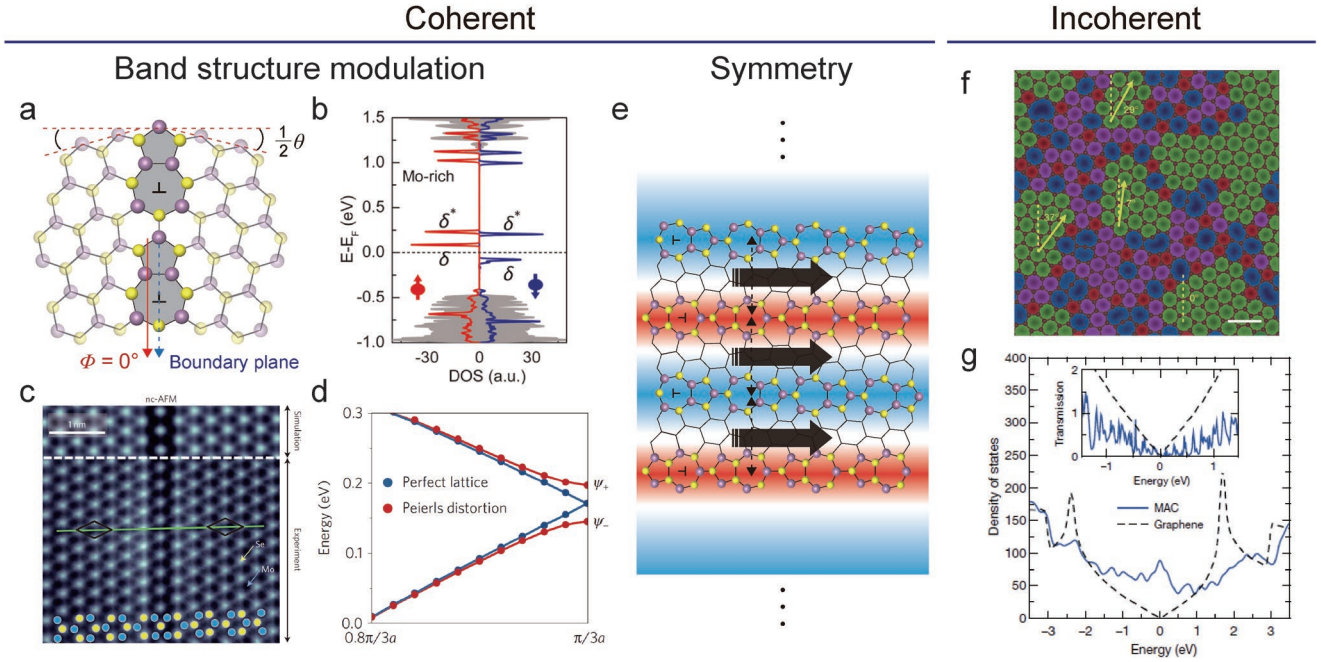

Figure 3. Stitching boundary-driven properties. a) Schematic of the atomic structure of coherent stitching boundaries (Mo 5|7 defect, purple circles: Mo atom, yellow circles: S atom), which are described with in-plane structural parameters, the tilt angle between merged domains, θ, and the inclination angle of the boundary, Φ. b) The spin-polarized density of states for isolated Mo 5|7 of MoS_2. Unlike the bulk region of MoS_2, mid-gap states near the Fermi level are newly formed by stitching boundary structures, as indicated by red and blue lines. The gray lines indicate the density of states in a monolayer MoS_2 perfect lattice. c) Non-contact atomic force microscopy image of monolayer $MoSe_2$ with mirror twin boundary. Se (Mo) atoms are presented in yellow (blue) circles. The Se atoms form an uninterrupted hexagonal lattice. In contrast, the Mo atoms switch their positions within the indicated unit cells of the Se between the two sides of the mirror twin boundary. d) Electronic band structure of the metallic state near the edge. The band gap modulation occurred when a Peierls distortion was introduced. e) Illustrating films with anisotropic conduction property by symmetric line defects of stitching boundaries. f) The theoretical atomic image of incoherent stitching boundary structure of monolayer amorphous carbon (MAC) without periodicity. Unlike coherent stitching boundary, the non-hexagonal rings (pentagon, heptagon, etc.) are randomly presented within monolayer film, which can emerge with different electronic properties. The scale bar is 0.2 nm. g) The density of states of the MAC (blue lines) shows a peak at the Fermi energy compared with that of graphene, a perfect crystal structure (black dotted lines). b) Reproduced with permission.[63] Copyright 2013, American Chemical Society. c,d) Reproduced with permission.[75] Copyright 2016, Springer Nature. f,g) Reproduced with permission.[78] Copyright 2020, Springer Nature.

dislocation is rotated by Φ from the hypothetical mirror plane between the two stitching domains, called the plane of symmetry.[61] The two parameters of θ and Φ determine the density of grain boundaries and the type of dislocation cores, respectively. To compensate for the lattice mismatch between the tilted domains, dislocation cores with a Burgers vector, $\vec{b}$, are formed with a density of d, dictated by $2/|\vec{b}|\sin\theta$, and the types of cores with different chemical bonds and shapes are determined by Φ, which is associated with the edge configurations of merging domains.[62] The key difference between the stitching and stacking boundaries is that the stitching boundaries involve strongly distorted covalent bonds at the interfaces to guide the possible atomic configurations. The boundary structure can be maintained once it is formed under controlled kinetic and energetic conditions.

The periodic arrays of dislocation cores placed close to interact strongly result in coherent electronic states with dispersive band topology and specific symmetry. For example, the symmetric tilt boundary between MoS_2 domains with a finite θ and $\Phi = 0°$ is shown in **Figure 3**a, where pairs of pentagon–heptagon (5|7) rings with a finite $\vec{b}$ are arranged. Symmetric dislocations with Φ = 0°, 30°, and 60° are the most preferred structures with evenly distributed dislocation cores to minimize the total strain energy by lattice distortions near the dislocation cores.[62] Precise control of Φ further results in deterministic formation of atomic structures for the dislocation cores, leading to novel properties. For instance, the stitching boundaries can be composed of an array of odd-membered rings (i.e., pentagon–heptagon rings) with homo-elemental bonds such as Mo—Mo or S—S bonds. When they have specific homo-elemental bonds only, either Mo—Mo or S—S bond, spin-polarized electronic states can emerge at different energy levels (Figure 3b).[20,63] Therefore, if the Fermi level is aligned between the spin-polarized states by a moderate doping, a net spin can be resulted in the structures. With a high enough density of cores at a high θ, the spin-polarized sates can be delocalized, enabling spin-polarized transports along the grain boundaries,[64] and also enhancing the exchange interactions, for an emergence of magnetic orderings.[63,65]

Another example of widely studied dislocation is a twin boundary with θ = 180° (Figure 3c,d). The dense periodic array of defects generates dispersive bands, realizing 1D conductors embedded in host materials, such as hBN,[66] TMDs,[67–72] and other 2D materials.[73,74] They are subject to various phenomena, expected in 1D conductors, including an ultra-narrow electric channel with high mobility,[74] spin, and

Table 3. Summary of engineering techniques for controlling stacking boundaries.

Method	Assembly unit	Available materials	Control parameter	Controllability	Scalability	Refs.
Automated assembly	CVD film	TMD	θ	±0.2°	≈0.01 mm^2	[110]
	Exfoliated flake	Gr, TMD, hBN		±1°	≈10 ~ 100 μm^2	[160]
	CVD film	Gr, hBN		±1°	≈25 cm^2	[106]
Manual assembly						
	CVD film	TMD		±0.1°	≈1 cm^2	[161]
	Exfoliated flake	Gr, TMD, hBN		±0.1°	≈0.01 mm^2	[48,49,97,98,151]
	Exfoliated flake	TMD	t		≈1 cm^2	[100]
Manual folding	Exfoliated flake or CVD film	Gr	θ	±1°	≈1 μm^2	[162,163]

charge density order.[75–77] While the current studies are mostly conducted in randomly obtained dislocations, if they can be fabricated over macroscopic sizes, controllably, material platforms for large-scale fabrications of functional devices can be realized. For example, if the density of dislocations is high to dominate the overall crystalline structures, closely packed arrays of dislocations with oriented cores (Figure 3e) could exhibit high anisotropy in thermal, electrical, and optical properties with unique electronic transports along the dislocation lines. There are also incoherent stitching boundaries, where various atomic defects are randomly arranged (Figure 1i). Films with dense boundaries of random atomic configurations result in completely amorphous structures[78] with insulating properties and low dielectric constants that are distinct from the crystalline counterparts (Figure 3f,g). The system has a larger entropy than the crystalline structure due to a higher structural degree of freedom with the absence of periodicity and symmetry.[79] We note that the amorphous structures are determined not purely by thermodynamics, which considers the entropy of the system. Instead, they are often kinetically determined. The amorphous structure is a meta-stable form with a large kinetic barrier for the transition toward the thermodynamically most stable, crystalline structure. Therefore, they are generally grown in low temperatures indicating that the structures are kinetically determined, instead of thermodynamics. In Table 2, we have listed several examples of various stitching boundaries and their properties, including both coherent and incoherent structures.

3. Stacking Boundary Engineering

Significant efforts have been made to develop manufacturing techniques for artificial vdW solids with interlayer control over the past decades. However, the fabrication techniques need to be improved in two aspects for the application of the discovered or proposed properties in the vdW solids. First, the production yield needs to be increased for mass production. Second, the precision for the control of the interfacial structural parameters needs to be improved for the reliable production of materials with uniform properties. To achieve the goals, the current existing methodologies in the self- and artificial-assembly approaches have their unique strengths; however, there are unresolved issues. Below, we review state-of-the-art techniques to form controlled interlayer structures. (**Table 3**)

3.1. Self-Assembly Approach

The self-assembly process of forming materials could be a powerful approach for the mass-production of 2D structures, as multilayer films over a large area can be grown without the complex layer-by-layer assembly steps.[80] In the growth of 2D materials using chemical vapor deposition (CVD), multilayer domains possess interlayer boundaries. For example, the perturbation of gas flows during the growth produces twisted multilayers with a finite θ by forming misaligned hetero-site nucleation for individual layers.[81] In addition, asymmetric mechanical stress during the growths produces stacking faults.[82] However, the interlayer boundaries are spatially non-uniform as the energy costs for transitions between different stacking orders are low by the weak vdW interlayer interactions. Several techniques have been developed for deterministic control of the structural parameters, θ and t.

First, to control θ, screw-dislocation-driven growths have been studied. As pictured in **Figure 4**a, when the crystal nucleates from a screw-dislocation center, a helicoidal structure is formed as the growth continues due to shear by sliding one layer vertically above the interfacing layer.[83] For a polar monolayer with broken inversion symmetry, the consecutive layers are oriented toward the same direction with $\theta = 0°$, maintaining the broken inversion symmetry, which is distinct from the energetically most stable AA′ stacking orders.[84–86] Furthermore, the θ can be arbitrarily tuned over a broad range by engineering the geometry of growth surfaces. The rotational polarity and magnitude of θ in Eshelby twist on flat surfaces are determined as $\theta = \vec{b}/r^2$, where $\vec{b}$ is the Burgers vector for screw dislocation and r is the radius of rotated crystals.[87,88] On the other hand, growths on curved surfaces produce multilayers with so-called supertwists (Figure 4a),[89] which can potentially make a full coverage on a non-Euclidean cone or hyperbolic cone surface (Figure 4b). For that, a part of flat circular film needs to be cut or added along the radius using an angle of α, respectively, which determines the θ of the twisted interfaces in the resultant helicoidal structures (Figure 4c). Therefore, by manipulating the shape of the surface between cone and hyperbolic cone, as well as the curvature of the surface, the rotational polarity and the magnitude of θ could be tunable over a broad range. The twisted materials can be scaled up as the θ of supertwists, driven by substrate geometry, is independent of the size of the crystals.

Second, for the control of t, both mechanical[90–93] and electric perturbations[94] can modify the local stacking orders. Applying

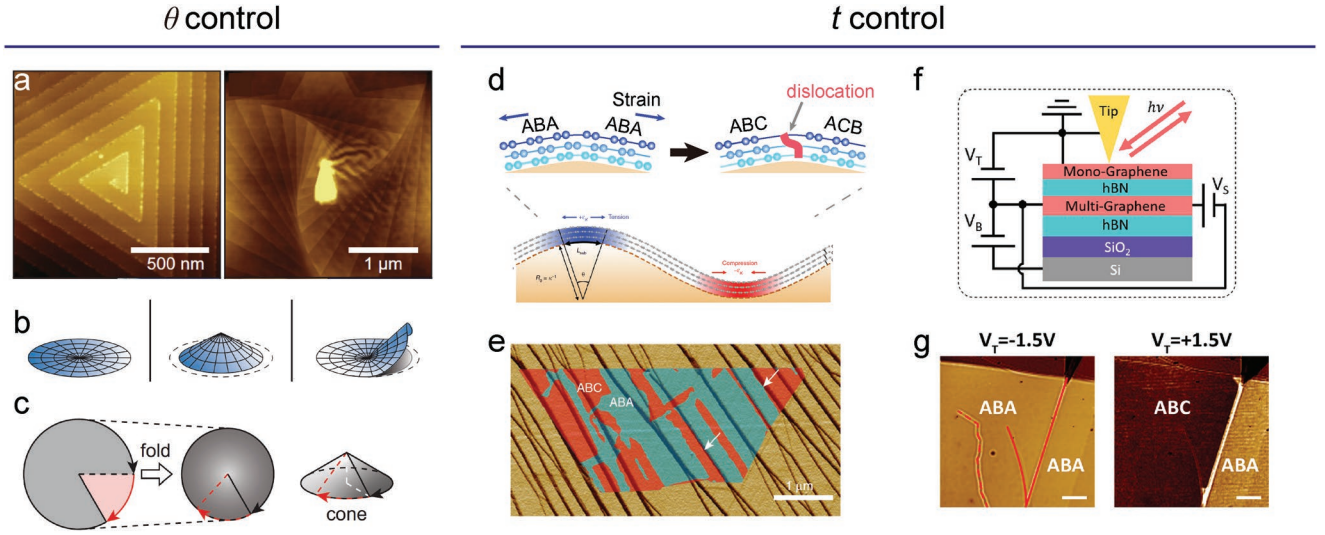

Figure 4. Representative methods for controlling stacking boundary during growths. a–c) Super twisted spiral growth for θ-controlled 2D crystals on non-Euclidean surfaces: a) Atomic force microscopy image of screw-dislocation driven spiral (left) and super twisted spiral (right) 2D crystals. b) Schematics of Euclidean (left) and non-Euclidean surfaces (middle and right). c) Schematics of transition from a flat surface to a cone by folding flat surface, which indicates that some parts of 2D films should be cut to fully cover the cone surface. d,e) Rhombohedral trilayer graphene growth on curved surfaces: d) Schematics of rhombohedral trilayer graphene on curvature. After the curvature induced stress is released, stacking order is changed from ABA to ABC (top). e) Atomic force microscopy amplitude image of trilayer graphene as-grown on substrates, overlapped with stacking order measured by dark-field transmission electron microscopy. f,g) Stacking order transition by displacement field and doping on dual-gate multilayer graphene devices: f) Schematic of the dual-gated few-layer graphene device with the infrared scanning nearfield optical microscopy measurement. When the displacement field is imposed on HG or RG, the thermodynamic ground state is changed from HG to RG by band gap opening only for RG. Then, the stacking order of graphene is changed from HG (ABA) to RG (ABC) to become more stable. g) Top gate voltage-dependent stacking order change of HG to RG with non-zero bottom gate voltage. The scale bar is 1 μm. a,b) Adapted and c) reproduced with permission.[89] Copyright 2020, American Association for the Advancement of Science. d) Reproduced and e) adapted under the terms of the CC-BY Creative Commons Attribution 4.0 International license.[93] Copyright 2020, the Authors. Published by Springer Nature. f,g) Adapted with permission.[94] Copyright 2021, American Chemical Society.

shear stress laterally to slide one layer with respect to the interfacing layer is the most apparent approach to change t.[90–92] The stress can occur during the growths of the crystals due to the interactions with the underlying substrates. For instance, multilayer graphene grown on rough surfaces experience local tensile or compressive stresses in each hillock and ditch (Figure 4d).[93] When the curvature-induced strain exceeds the formation energy for stacking faults, transitions of the crystalline structures can occur to change the hexagonal structure to the rhombohedral structure without any post-process (Figure 4e).

Alternatively, the growth of multilayer graphene with controlled stacking fault has been demonstrated on composition-modulated growth substrates. On Cu–Si alloy substrates, the four-layer graphene shows rhombohedral stacking order with a high yield of over 80% with characteristic band structures, confirmed by angle-resolved photoemission spectroscopy.[95] While the underlying mechanism is unclear, an independent study suggests that the displacement field, induced by the underlying substrate is the reason for the formation of rhombohedral multilayers, whose electronic energy is lower than that of natural hexagonal crystals under the field (Figure 4f,g).[94]

3.2. Artificial Assembly Approach

A different approach to forming controlled stacking boundaries is based on artificial assembly, where separate 2D materials are assembled layer-by-layer. There are several unique advantages of this approach over the self-assembly techniques. First, once the reliable production of building blocks is possible, various interlayer boundaries can be produced in the same process by simply changing the stacking configurations. Second, one can fabricate structures that are thermodynamically difficult to obtain from growths. For instance, twisted bilayer graphene with a low θ tends to transform into the energetically most stable stacking orders with $\theta = 0°$ at high-temperature growths,[96] resulting in a low yield of production.[82] However, an artificial assembly can readily provide the structures.[97,98] Finally, in multilayer stacks, each interface is individually programmable to arbitrarily realize various stacking orders, including periodic, aperiodic, and quasi-crystalline along the out-of-plane direction, which is not currently possible by self-assembly approaches.

We have summarized the developments of the assembly techniques in **Figure 5**a. There are three key technical requirements for reliable fabrications of controlled interfaces. First, we should produce crystalline building blocks on a large scale. Second, the atomically clean assembly should be possible. Third, the assembly process needs to be automated for the high throughput of the products.

For the assembly units, exfoliated crystals have been a major source as the process requires only bulk crystals and adhesive tapes. So-called "pick-up" method was developed,[13,99] where exfoliated crystals are assembled by vdW

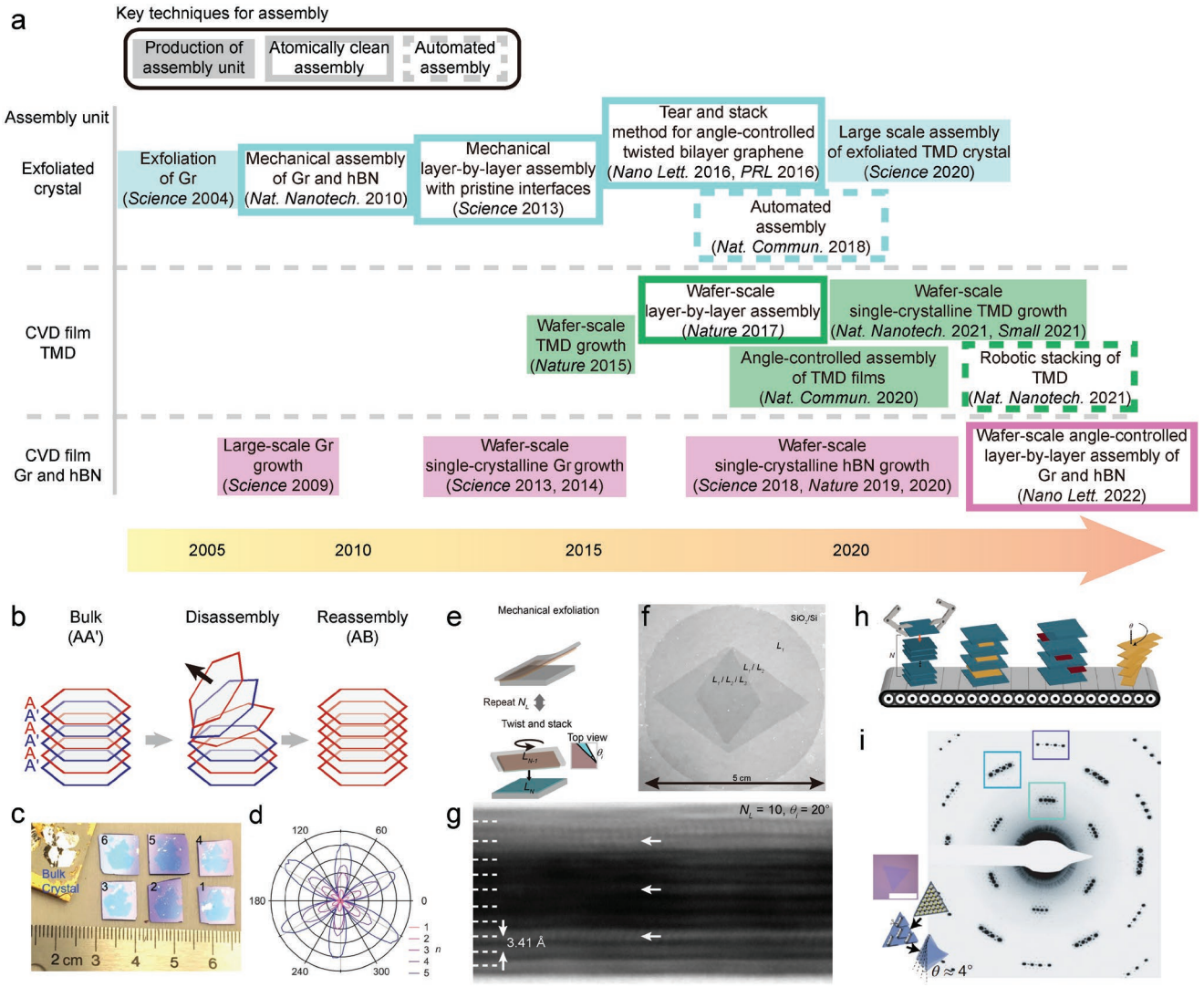

Figure 5. Representative methods for controlling stacking boundary using assembly methods. a) Summary of 2D assembly development. b–d) Cm-scale exfoliation of monolayer TMD films from bulk crystals and fabrication of artificial AB-stacked multilayer TMD films: b) Schematics of the artificial AB stacked crystals assembly technique. Bulk crystals (AA′) are composed of two 180° rotated repeating units. The same repeating units (odd or even pairs) are collected and reassembled one by one to form AB stacked crystals. c) Optical image of sequentially exfoliated cm-scale monolayer films in the same bulk crystals. d) Angle-resolved second harmonic generation intensity plots. The second harmonic generation intensities show quadratic enhancement by increasing the number of layers stacked. e–g) Wafer-scale angle-controlled assembly of single-crystalline oriented graphene and hBN for twisted multilayer films: e) Schematics of the angle-controlled assembly process. Graphene or hBN films are grown epitaxially on single-crystal germanium substrates. The films are picked up and stacked to the next films with rotation based on the substrate's edge. f) Image of wafer-scale twisted trilayer graphene films. g) Annular dark-field scanning transmission electron microscopy image for cross section of twisted multilayer graphene. h,i) Robotic assembly of 2D materials. h) Schematics of robotic assembly. Patterned 2D materials are assembled to form a twisted multilayer structure. i) Diffraction pattern of constantly twisted four-layer WS_2. Satellite peaks are observed, indicating that a large-scale periodic structure is overlaid on all interfaces. c,d) Reproduced with permission.[100] Copyright 2020, American Association for the Advancement of Science. e–g) Adapted with permission.[106] Copyright 2022, American Chemical Society. h) Adapted and i) reproduced with permission.[110] Copyright 2022, Springer Nature.

interactions to form atomically clean interfaces, and it became a standard method to fabricate controlled interfaces.[13] Techniques based on adhesives of metallic films have been developed to exfoliate large-scale crystals with deterministic control of the thickness (Figure 5b–d).[100,101] However, the size and production yield are not enough for the direct applications of the materials.

The scalability can be extended using CVD-grown films as the assembly unit. Various 2D materials have been made using epitaxial growths to yield a uniform thickness, low atomic defects, and single crystallographic orientation over wafer scales.[10–12,102–104] For the films to be suitable for the atomically clean assembly using the "pick-up" method, the interaction energy between the growth substrate and as-grown films needs to be lower than the vdW interactions between assembly units.[105,106] For instance, single-crystalline graphene and hBN films are bound to the epitaxy substrate; therefore, chemical etching of the substrate is required to isolate the 2D films,

which contaminate the interfaces.[107] A recent study shows that single-crystalline graphene and hBN monolayers grown on Ge(110) substrates can be assembled, assisted by vdW interactions, to form wafer-scale films of pristine interfaces with near-unity yield (Figure 5e,f).[106] The θ of each interface in the films is tailored with layer-resolved in-plane crystalline orientations (Figure 5g). This approach also allows the reuse of the growth substrate after assembly. There are numerous other 2D materials, which are waiting to be grown on a large scale for assembly. In particular, there are many 2D materials, whose in-plane rotational symmetries are different from the most widely studied crystals with three- or six-fold symmetries, and their symmetries can result in qualitatively different properties. As examples, there are materials with a rectangular lattice of twofold symmetry,[108] such as GeSe, GeS, and black phosphorene. The monolayer structures show anisotropic electrical and optical conductivities along the in-plane directions by the intrinsic symmetry. Interestingly, when twisted structures with a finite twist angle, θ are fabricated, new topological lattices with effective 1D arrays can be demonstrated.[109] Because the supercells in the emerging moiré pattern are also rectangular in low θ, the reduced hopping parameters by the enlarged unit cells result in dispersionless bands along only one direction, realizing a novel artificial platform of topological mosaic with 1D arrays. Finding the right epi-substrate to fulfill the aforementioned requirements (Figure 5e) will be the first step to realizing the reliable assembly for the target 2D materials. Finally, the production yield can increase by automating the layer-by-layer assembly process, as demonstrated in a recent study, where large-scale TMDs grown using the CVD are automatically assembled to manufacture vdW solids with determined θ and number of layers (Figure 5h,i).[110]

4. Stitching Boundary Engineering

Intralayer boundaries in vdW materials result from direct chemical bonds for lateral stitching of misoriented domains; therefore, their formations require growth steps. During the growths, the intralayer structural parameters, θ and Φ, are set using boundary conditions of the merging domains. Similar to the cases of stacking boundaries, we classify the techniques to engineer the boundary conditions into two categories of self- and artificial-assembly approaches, depending on if manual manipulation of individual domains is involved in the process.

4.1. Self-Assembly Approach

In the self-assembly approach, the stitching boundary structures are spontaneously determined by changing the growth conditions. Engineering growth substrates, such as surface topography and crystallographic orientation, is an efficient way to affect the crystalline structures of 2D materials. Tilted boundaries with a designed θ to determine the density of dislocation cores in the final product can be obtained using growths on nonplanar substrates with positive Gaussian curvature, described as the opening angle, α in a conical shape (**Figure 6**a, left).[111,112] The single-crystalline film is grown along the surface curvature (Figure 6a, inset image). As two growth front propagates along the curved surface, they merge by forming grain boundaries.[111] Thus, the θ of the tilted boundaries is determined using the topographic shape of the substrate, following the relationship of $\theta = 2\pi\,(1 - \sin(\alpha/2))$ (Figure 6a, right), as demonstrated in the growth of monolayer WS_2 with tilted boundaries on curved single-crystalline Si substrates.[112] This approach is, in fact, similar to the method to control twisted interlayer boundaries; however, the difference is that the growth occurs in a high condensation regime, where lateral stitching is preferred.[113]

In a different approach, the θ can be set by individual control of crystalline orientation for merging domains. Epitaxial growth on single-crystalline substrates can allow directional growth of 2D materials. Therefore, if the crystalline orientation of the epi-substrate can be spatially programmed, predesigned θ can be obtained by merging domains with controlled crystalline orientations. Although such a growth template has not been realized for 2D materials, epitaxial growths of 2D materials on various substrates have been widely studied and can provide a guideline for selecting the right substrates to develop the template. For the grown domains to have a specific crystalline orientation, there are two conditions. First, the symmetry group of 2D materials should contain that of substrates.[114] When the substrate has a C_n rotational symmetry, the 2D material should also have the C_n rotational symmetry to be uni-directionally aligned. For instance, on a substrate with C_2 symmetry, vdW materials with C_4 and C_6 symmetries can be aligned; however, not the one with C_3 symmetry, where the C_2 symmetry is absent (Figure 6b). Second, the high symmetric mirror plane of 2D material needs to be aligned to that of the underlying substrate in the energetically most stable configurations.[103,104,115,116] If the high-symmetric line of the 2D material is grown toward the low-symmetric directions of the substrate, there will be an orientation variety. In theory, if we choose the right epi-substrate, we can form the growth template by combining pixelated domains of substrates with controlled crystalline orientation. We will discuss this further in the challenges and outlook section.

To control θ in the tilted boundaries of polycrystalline films, we can use an epi-substrate, on which the 2D materials are aligned toward several orientations.[117] For instance, if the 2D film is thermodynamically aligned toward the two different orientations of the growth substrate (Figure 6b, right inset) that are tilted by α, we will have polycrystalline films with controlled grain boundaries, represented by the tilt angle of θ that is equal to α.[118] Therefore, one can realize a macroscopic film with determined grain boundaries and specific θ to obtain a target property.[20,63,66,119,120] For instance, twin boundaries with $\theta = 180°$ can be formed to present metallic conduction.[118]

4.2. Artificial Assembly Approach

Engineering intralayer boundaries is possible by manipulating the merging domains to form grain boundaries. The design and fabrication of grain boundaries are possible through the "quasi-bicrystal nanowelding approach".[122] The nanowelding approach proceeds in the following order. First, two single-crystalline films are twisted and stacked with a specific twist angle.

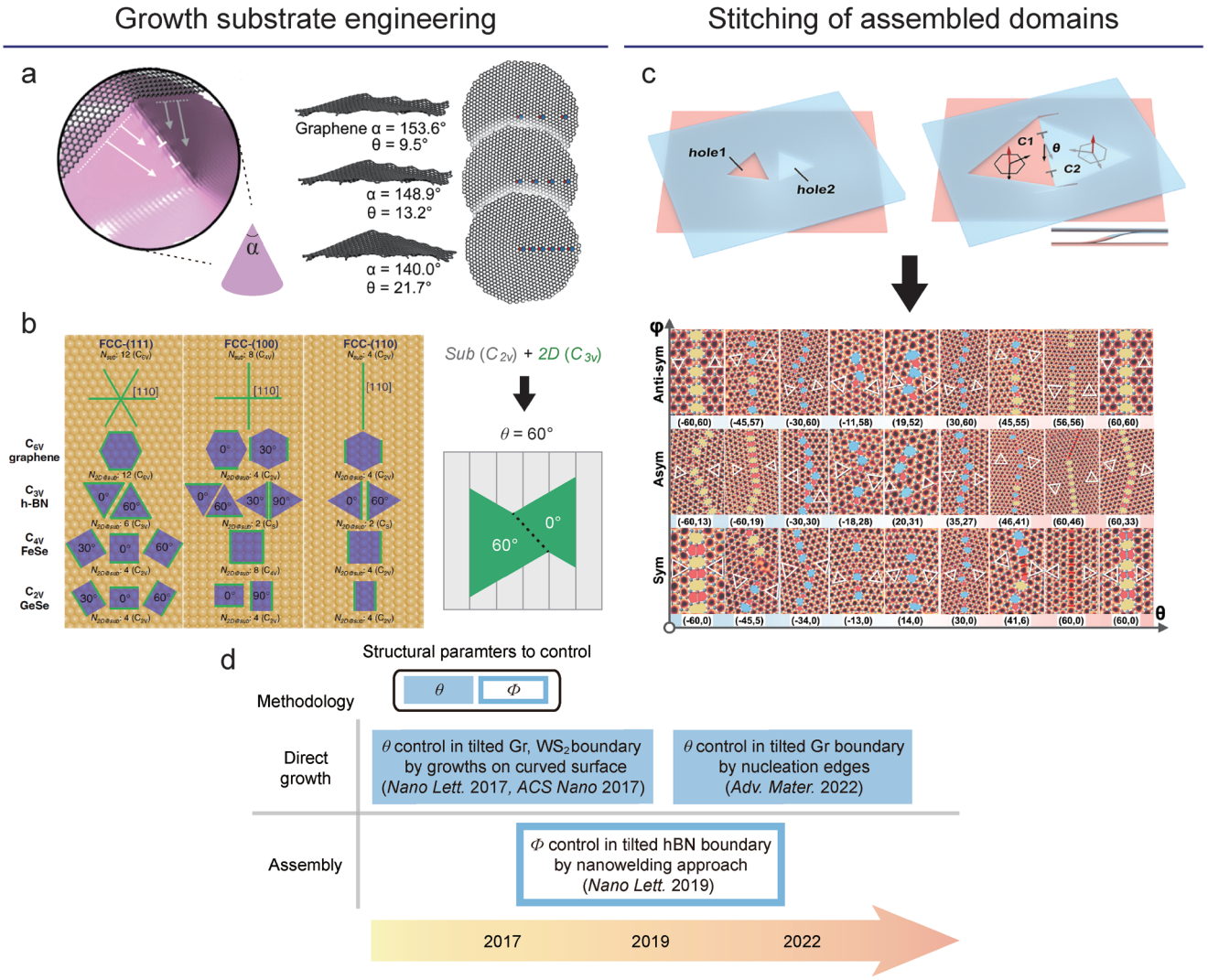

Figure 6. Techniques for engineering stitching boundaries. a) The structure of the conical growth substrate with an opening angle, α. It shows that the tilt angle, θ changes as the substrate's curvature, resulting in a difference in dislocation density. b) The schematics for the alignment of 2D materials with various symmetries on low-index fcc surfaces. It shows the results of the interplay between 2D materials and substrates with different symmetry groups, where the symmetry group of the substrates is a subgroup of that of the 2D materials. For instance, only one type of boundary with $\theta = 60°$ occurs by the interplay between C_{2v} substrate (gray line) and C_{3v} 2D materials (green triangle). c) The illustration for the fabrication of stitching boundary by stitching assembled domains. By this process, the grain boundaries with controlled in-plane structural parameters are experimentally achieved, resulting in different stitching boundary structures. d) A summary for the developments of the key techniques to control the structural parameters for stitching boundaries. a) Adapted with permission.[111] Copyright 2017, American Chemical Society. b) Reproduced under the terms of the CC-BY Creative Commons Attribution 4.0 International license.[114] Copyright 2020, Springer Nature. c) Adapted with permission.[122] Copyright 2019, American Chemical Society.

Second, nanosized holes are generated on the bottom and top layers of each film using electron beam irradiation and stitched (Figure 6c, top). With the spherical aberration-corrected electron optics, the location and size of the holes can be controlled to the atomic level. Through this approach, the stitching boundaries of hBN change with different atomic structures, depending on θ (Figure 6c, bottom).

The aforementioned methods control θ; however, we must control Φ for deterministic control of electronic structures and properties, associated with the types of atomic defects at the dislocation cores.[17,20,72,123] The Φ is set by the merging edge configurations of the domains.[123,124] To control the edge configurations, several approaches can be used, including modulations of chemical potentials during the growth by changing substrates[117,125] and growth environments.[126–129]

We have made a summary for the developments of the techniques to control the structural parameters of stitching boundaries, θ and Φ, which determine the final atomic structures at the boundaries(**Table 4**, Figure 6d). While many theoretical studies[124,130,131] predict peculiar atomic structures and their properties, expected at specific θ and Φ, structural control techniques been much less developed than the case of stacking boundaries in terms of controlling the structural parameters, and there are only a few experimental demonstrations. Most of the previous studies for controlling the stitching boundaries discuss the modulations of macroscopic

Table 4. Summary for engineering techniques for controlling stitching boundary.

Method	Control parameter	Materials	Refs.
Growth on curved surfaces	θ	Gr, TMD	[111,112,124]
Growth on symmetry-controlled substrates		All 2D	[114,118]
Stitching of assembled domains	Φ	hBN	[122]

shapes of boundaries and their properties,[132–135] rather than the boundary structures at the atomic scale, and arbitral control of θ and Φ is difficult, and only limited boundary structures such as twin boundaries with $\theta = 180°$[67,75–77,121,134,136] have been realized.

5. Challenges and Outlook

Here, we summarize the remaining challenges and outlook for controlling stacking and stitching boundaries in 2D materials.

5.1. Stacking Boundaries

The method to design stacking boundaries can be a powerful tool to program the electronic properties of 2D materials. Numerous artificial solids could be fabricated, even in a single material platform, using a design approach with atomic-level precision on a technologically relevant scale, facilitating the discovery of various physical properties and advanced functional nanodevices. However, for that, the current issues in both self- and artificial-assembly approaches need to be resolved. We need better structural controllability in the self-assembly approach and higher throughput for the artificial assembly.

First, in the self-assembly approach, to control t for deterministic formations of stacking faults, a more robust driving force is required to guide their structures. Thus, asymmetric bound conditions could be set across the multilayer films by sandwiching them with dissimilar materials (**Figure 7**a–c), inducing out-of-plane displacement fields. For multilayer graphene, rhombohedral structures could be spontaneously driven by reducing electronic energy using a band gap opening (Figure 7b).[16,94] This strategy could be used for engineering polar structures (Figure 7c) as it is energetically preferred for the rhombohedral structure to have a particular stacking configuration to align the spontaneously formed net dipole in the film to the displacement field. If one can find a combination of encapsulation materials that can produce a sufficient displacement field with the capability to control the number of layers, this approach will be useful for manufacturing 2D materials.

Second, to control θ in the screw-dislocation-induced growth, the substrate morphology should be homogeneous, and the nucleation site needs to be well-defined. It is important to manipulate the curvature of the underlying surface to induce the supertwist with a predetermined magnitude of θ (Figure 7d). For the rotational polarity, determined by the Burger's vector direction of the screw-dislocation and the sign of the surface curvature, the screw-dislocation direction needs to be guided somehow and the nucleation sites should be placed either on the cone or near the cone (i.e., hyperbolic surface). Implanting nucleation seeds[137,138] on a chiral growth substrate with engineered surface topography could be an efficient way to achieve this goal.

In the artificial assembly approach, the main issue is how to increase the throughput. Considering that, the current bottleneck for the fabrication rate is the slow growth. The assembly units need to be produced faster in a larger quantity. A powerful way to increase the growth rate is using catalysts.[139–141] To increase the total speed of the processes, ideally, the materials could be grown on the same substrates right after the assembly, then resupplied in a single chamber, where the growth and assembly tools are combined. In addition, the growth of assembly units and interface engineering technology needs to be further developed to have a quality comparable to that of exfoliated crystals. We must achieve the growth of truly single-crystal materials[142] and high-quality insulating crystals for the handling layer[143] on a large scale.

These two methods complement each other and contribute to the development of new 2D electronic materials and devices based on boundary properties. For example, assembly units, fabricated in a self-assembly approach could be assembled to produce a new structure, and artificially assembled structures could be used as grwoth substrates to guide the growth by the self-assembly.

5.2. Stitching Boundaries

Precisely controlled assembly of domains within the 2D layer provides an exciting route to design artificial solids with a wide range of tunability. We call the new material design platform "2D mosaic patterns" because the final 2D material is made up of pieces of assembly units. The assembly domains can be tailored to have a variety of sizes and shapes, and form superlattices with a wide range of morphologies from network structure to the directional linear pattern, where dense arrays of specific intralayer boundaries are formed in a predefined geometry (**Figure 8**a). When the density of domain boundaries is high, the electronic states of the boundaries govern the macroscopic electrical properties of the artificial solid, resulting in a variety of designer functionalities, such as high electron mobility in conducting 1D network (Figure 8c, top), and anisotropic electrical and thermal conductions in linear dislocation array (Figure 8c, bottom). Furthermore, when the size of assembly units is comparable to the characteristic dimension for a specific property (e.g., the exciton radius of 1–3 nm in 2D semiconductors,[144,145]), the related electronic state and the property will be significantly altered by the boundary conditions of a specific shape. Individual domains' local states can interact with each other to generate new collective electronic states in the superlattices, resulting in emergent phenomena.

Methods to realize 2D mosaic patterns can be categorized into two subgroups. The first "assembly and stitching" approach involves the assembly of 2D domains with designed shapes via lithography or direct growth,[117,146] followed by another growth in a controlled environment to fill gaps between domains

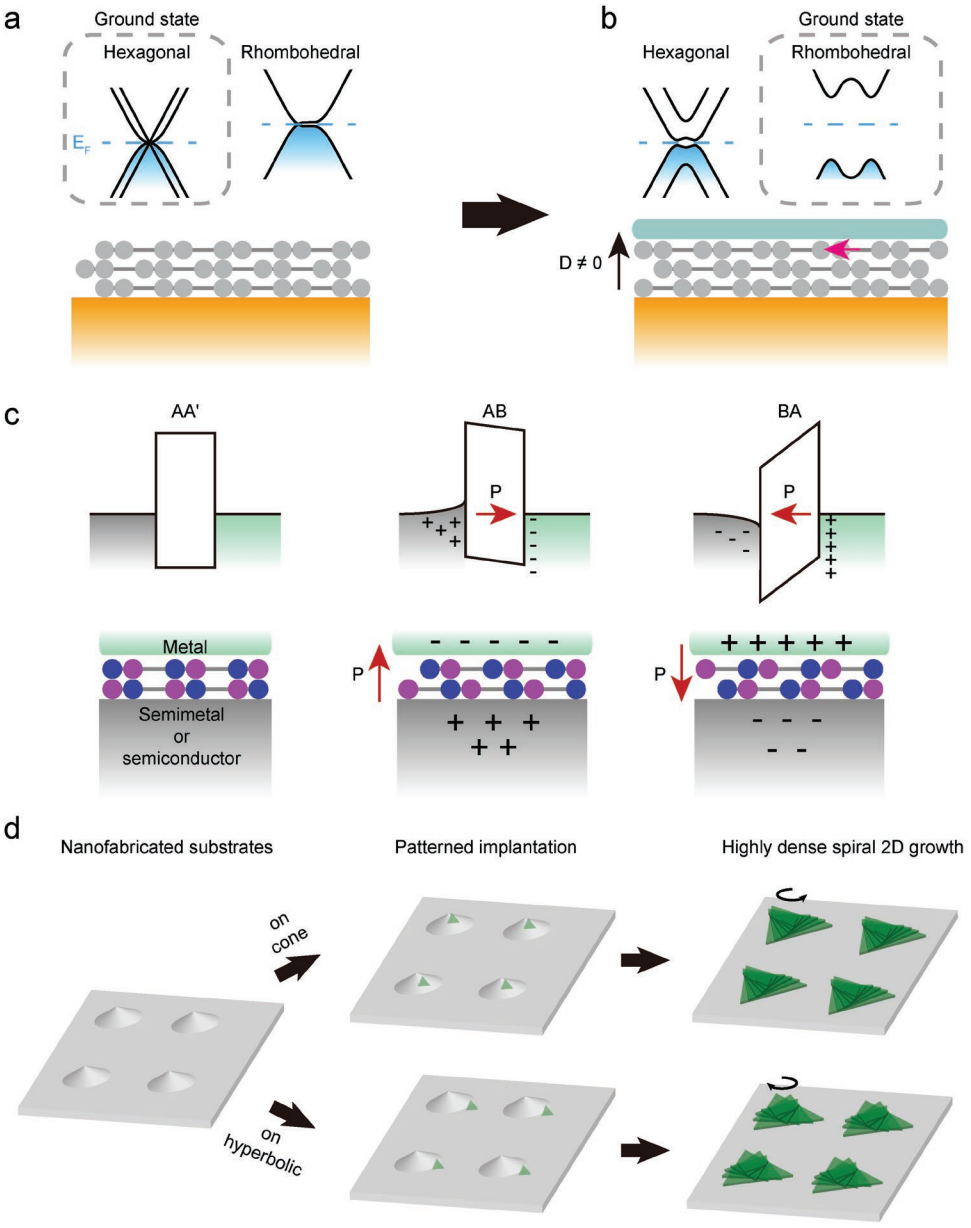

Figure 7. Methods for controlling stacking boundary by engineering the topology and composition of substrates. a–c) Stacking order control of multilayer graphene and 2D polar films with asymmetric interfaces: a) Schematics for as-grown trilayer graphene on growth substrates, with stacking order-dependent band structures. HG is the ground state on as-grown substrates. However, when displacement field is imposed by b) asymmetric interfaces, ground states change from HG to RG with band gap opening. c) Schematics of the interface and band structure of 2D polar films with different screen lengths between metal and semimetal (or semiconductor). The asymmetric depolarization field induces additional electrostatic potential change when the films exhibit ferroelectricity (BA or AB stacking order), producing BA stacking as ground states. d) Growth method for θ controlled 2D materials. Nanofabrication method carefully designs the curvature of growth substrates, and patterned 2D films are implanted on the surface, cone or hyperbolic. Then, highly dense, θ and chirality controlled-spiral 2D films are grown.

for lateral stitching.[147] In the second approach of "patterned growth," the targeted superlattice structure is directly grown on an epi-growth template, in which the crystalline orientations are spatially programmed (Figure 8a). While such a template has not yet been realized, the 2D mosaic pattern obtained through the assembly and stitching method could realize the growth template. Importantly, once constructed, the template can be reused for multiple growths.

The material design concept of 2D mosaic patterns could be classified as supermolecule engineering, in which molecular-level units are designed to provide predictable structure in the final aggregates, such as in the case of metal–organic frameworks. However, the 2D mosaic pattern has several advantages over other material systems for producing electronic components for several reasons. First, the in-plane structure is robust, as constructed with strong covalent bonds. Second, it has an

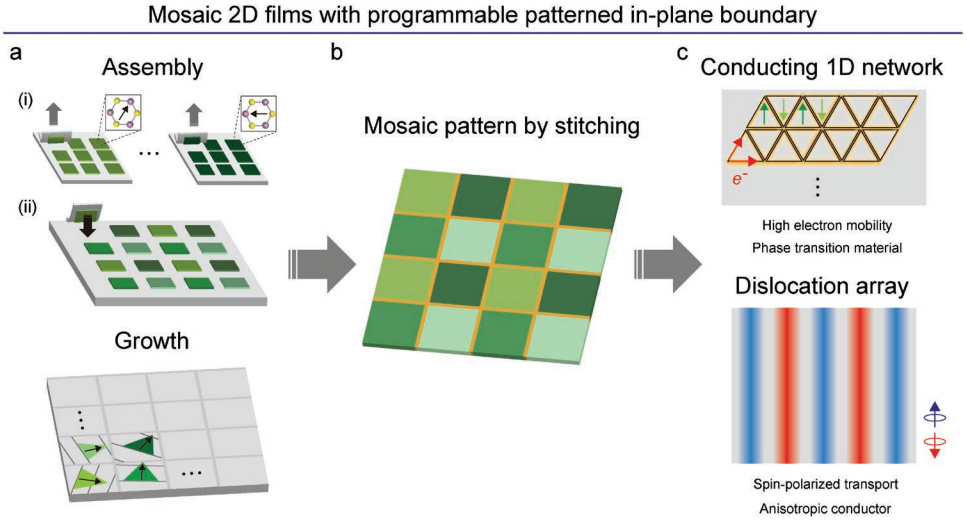

Figure 8. Perspective overview of Mosaic 2D films with the programmable patterned stitching boundary. a) The illustration of technical methods for Mosaic 2D films. The mosaic pattern can be prepared by either assembly (top) or direct growth (bottom). For the assembly method, (i) assembly units are first grown and patterned. (ii) Then, the units with different in-plane crystallographic orientations are assembled on a target substrate with position control. For the direct growth method, pre-designed growth substrates, in which the crystalline orientations are spatially programmed, are used. b) Mosaic 2D films are stitched between misaligned domains by the technique such as assembly or growth. c) Illustrations of novel Mosaic patterns such as conducting 1D network and dislocation array. Conducting a 1D network can be realized by an array of metallic twin boundaries (yellow highlighted lines), resulting in 2D materials with high electrical transport and phase transition properties. A dislocation array can present anisotropic conduction properties, as shown in Figure 3e. Additionally, if the dislocation has a spin-polarized system depending on the type of dislocation core, it can be used as a device with spin-polarized transport in spintronics.

extensive structural degree of freedom as the shape of assembly units can be arbitrarily designed, and the tilted boundaries can be also engineered to modulate the interdomain interactions. Finally, it has outstanding electrical and optical properties, such as high electrical conductivity and strong light absorption.

5.3. Conclusions

2D materials have been highlighted as ideal low-dimensional materials for realizing advanced electronic devices and novel quantum devices. To obtain intrinsic properties expected from perfect crystal structures, great technological progresses have been made to minimize crystalline imperfections, including grain boundaries. Meanwhile, exotic properties discovered in various boundary structures of 2D materials suggest the possibility of realizing novel functional devices. The majority of structural boundary research, however, is still limited to fundamental studies on their physical properties and small-scale demonstrations of the structures. Groundbreaking technological advances in the design of the boundaries at the atomic scale will open an exciting era in 2D electronic materials by enabling fabrications of artificial 2D solids with high scalability and reproducibility.

Acknowledgements

S.-J.Y. and M.-Y.C. contributed equally to this work. This work was supported by National R&D Program through the National Research Foundation of Korea (NRF) funded by Ministry of Science and ICT (2020R1C1C1014590, 2020R1A4A1019455, 2018M3D1A1058793, 2020M3D1A1110548, and 2022M3H4A1A01012718) and Institute for Basic Science (IBS) under Project Code IBS-R034-D1.

Conflict of Interest

The authors declare no conflict of interest.

Keywords

dislocation, grain boundaries, stacking orders, tilt boundaries, twist boundaries, two-dimensional materials, van der Waals structures

Received: April 15, 2022
Revised: June 30, 2022
Published online:

[1] S. Das, A. Sebastian, E. Pop, C. J. McClellan, A. D. Franklin, T. Grasser, T. Knobloch, Y. Illarionov, A. V. Penumatcha, J. Appenzeller, Z. Chen, W. Zhu, I. Asselberghs, L.-J. Li, U. E. Avci, N. Bhat, T. D. Anthopoulos, R. Singh, *Nat. Electron.* **2021**, *4*, 786.
[2] X. Liu, M. C. Hersam, *Nat. Rev. Mater.* **2019**, *4*, 669.
[3] G. Iannaccone, F. Bonaccorso, L. Colombo, G. Fiori, *Nat. Nanotechnol.* **2018**, *13*, 183.
[4] M. Chhowalla, D. Jena, H. Zhang, *Nat. Rev. Mater.* **2016**, *1*, 16052.
[5] M. Amani, D.-H. Lien, D. Kiriya, J. Xiao, A. Azcatl, J. Noh, S. R. Madhvapathy, R. Addou, K. C. Santosh, M. Dubey, K. Cho, R. M. Wallace, S.-C. Lee, J.-H. He, J. W. Ager, X. Zhang, E. Yablonovitch, A. Javey, *Science* **2015**, *350*, 1065.
[6] Y. Liu, X. Duan, H.-J. Shin, S. Park, Y. Huang, X. Duan, *Nature* **2021**, *591*, 43.
[7] J.-H. Park, S.-J. Yang, C.-W. Choi, S.-Y. Choi, C.-J. Kim, *ACS Appl. Mater. Interfaces* **2021**, *13*, 22828.
[8] Y. Liu, Y. Huang, X. Duan, *Nature* **2019**, *567*, 323.
[9] H. Kum, D. Lee, W. Kong, H. Kim, Y. Park, Y. Kim, Y. Baek, S.-H. Bae, K. Lee, J. Kim, *Nat. Electron.* **2019**, *2*, 439.

[10] J. H. Lee, E. K. Lee, W. J. Joo, Y. Jang, B. S. Kim, J. Y. Lim, S. H. Choi, S. J. Ahn, J. R. Ahn, M. H. Park, C.-W. Yang, B. L. Choi, S. W. Hwang, D. Whang, *Science* **2014**, *344*, 286.
[11] J. S. Lee, S. H. Choi, S. J. Yun, Y. I. Kim, S. Boandoh, J. H. Park, B. G. Shin, H. Ko, S. H. Lee, Y. M. Kim, Y. H. Lee, K. K. Kim, S. M. Kim, *Science* **2018**, *362*, 817.
[12] L. Wang, X. Z. Xu, L. N. Zhang, R. X. Qiao, M. H. Wu, Z. C. Wang, S. Zhang, J. Liang, Z. H. Zhang, Z. B. Zhang, W. Chen, X. D. Xie, J. Y. Zong, Y. W. Shan, Y. Guo, M. Willinger, H. Wu, Q. Y. Li, W. L. Wang, P. Gao, S. W. Wu, Y. Zhang, Y. Jiang, D. P. Yu, E. G. Wang, X. D. Bai, Z. J. Wang, F. Ding, K. Liu, *Nature* **2019**, *570*, 91.
[13] L. Wang, I. Meric, P. Y. Huang, Q. Gao, Y. Gao, H. Tran, T. Taniguchi, K. Watanabe, L. M. Campos, D. A. Muller, J. Guo, P. Kim, J. Hone, K. L. Shepard, C. R. Dean, *Science* **2013**, *342*, 614.
[14] T. Hallam, S. Monaghan, F. Gity, L. Ansari, M. Schmidt, C. Downing, C. P. Cullen, V. Nicolosi, P. K. Hurley, G. S. Duesberg, *Appl. Phys. Lett.* **2017**, *111*, 203101.
[15] C. Jin, E. Y. Ma, O. Karni, E. C. Regan, F. Wang, T. F. Heinz, *Nat. Nanotechnol.* **2018**, *13*, 994.
[16] C. H. Lui, Z. Li, K. F. Mak, E. Cappelluti, T. F. Heinz, *Nat. Phys.* **2011**, *7*, 944.
[17] O. V. Yazyev, S. G. Louie, *Nat. Mater.* **2010**, *9*, 806.
[18] G. Li, A. Luican, J. M. B. L. dos Santos, A. H. C. Neto, A. Reina, J. Kong, E. Y. Andrei, *Nat. Phys.* **2010**, *6*, 109.
[19] H. Yoo, R. Engelke, S. Carr, S. A. Fang, K. Zhang, P. Cazeaux, S. H. Sung, R. Hoyden, A. W. Tsen, T. Taniguchi, K. Watanabe, G. C. Yi, M. Kim, M. Luskin, E. B. Tadmor, E. Kaxiras, P. Kim, *Nat. Mater.* **2019**, *18*, 448.
[20] X. Zou, Y. Liu, B. I. Yakobson, *Nano Lett.* **2013**, *13*, 253.
[21] D. M. Kennes, M. Claassen, L. Xian, A. Georges, A. J. Millis, J. Hone, C. R. Dean, D. N. Basov, A. N. Pasupathy, A. Rubio, *Nat. Phys.* **2021**, *17*, 155.
[22] D. Rhodes, S. H. Chae, R. Ribeiro-Palau, J. Hone, *Nat. Mater.* **2019**, *18*, 541.
[23] S. E. Kim, F. Mujid, A. Rai, F. Eriksson, J. Suh, P. Poddar, A. Ray, C. Park, E. Fransson, Y. Zhong, D. A. Muller, P. Erhart, D. G. Cahill, J. Park, *Nature* **2021**, *597*, 660.
[24] N. Kondekar, M. G. Boebinger, M. Tian, M. H. Kirmani, M. T. McDowell, *ACS Nano* **2019**, *13*, 7117.
[25] R. Bistritzer, A. MacDonald, *Proc. Natl. Acad. Sci. USA* **2011**, *108*, 12233.
[26] Y. Cao, V. Fatemi, A. Demir, S. Fang, S. L. Tomarken, J. Y. Luo, J. D. Sanchez-Yamagishi, K. Watanabe, T. Taniguchi, E. Kaxiras, R. C. Ashoori, P. Jarillo-Herrero, *Nature* **2018**, *556*, 80.
[27] R. W. Havener, Y. Liang, L. Brown, L. Yang, J. Park, *Nano Lett.* **2014**, *14*, 3353.
[28] H. Patel, L. Huang, C.-J. Kim, J. Park, M. W. Graham, *Nat. Commun.* **2019**, *10*, 1445.
[29] J. Yin, H. Wang, H. Peng, Z. Tan, L. Liao, L. Lin, X. Sun, A. L. Koh, Y. Chen, H. Peng, Z. Liu, *Nat. Commun.* **2016**, *7*, 10699.
[30] K. Liu, L. Zhang, T. Cao, C. Jin, D. Qiu, Q. Zhou, A. Zettl, P. Yang, S. G. Louie, F. Wang, *Nat. Commun.* **2014**, *5*, 4966.
[31] J. R. Schaibley, H. Yu, G. Clark, P. Rivera, J. S. Ross, K. L. Seyler, W. Yao, X. Xu, *Nat. Rev. Mater.* **2016**, *1*, 16055.
[32] Y. Cao, V. Fatemi, S. Fang, K. Watanabe, T. Taniguchi, E. Kaxiras, P. Jarillo-Herrero, *Nature* **2018**, *556*, 43.
[33] A. L. Sharpe, E. J. Fox, A. W. Barnard, J. Finney, K. Watanabe, T. Taniguchi, M. A. Kastner, D. Goldhaber-Gordon, *Science* **2019**, *365*, 605.
[34] P. Stepanov, I. Das, X. Lu, A. Fahimniya, K. Watanabe, T. Taniguchi, F. H. L. Koppens, J. Lischner, L. Levitov, D. K. Efetov, *Nature* **2020**, *583*, 375.
[35] L. Balents, C. R. Dean, D. K. Efetov, A. F. Young, *Nat. Phys.* **2020**, *16*, 725.
[36] N. P. Wilson, W. Yao, J. Shan, X. Xu, *Nature* **2021**, *599*, 383.
[37] C. N. Lau, M. W. Bockrath, K. F. Mak, F. Zhang, *Nature* **2022**, *602*, 41.
[38] Y. Shi, S. Xu, Y. Yang, S. Slizovskiy, S. V. Morozov, S. K. Son, S. Ozdemir, C. Mullan, J. Barrier, J. Yin, A. I. Berdyugin, B. A. Piot, T. Taniguchi, K. Watanabe, V. I. Fal'ko, K. S. Novoselov, A. K. Geim, A. Mishchenko, *Nature* **2020**, *584*, 210.
[39] J. Yang, G. Chen, T. Han, Q. Zhang, Y.-H. Zhang, L. Jiang, B. Lyu, H. Li, K. Watanabe, T. Taniguchi, Z. Shi, T. Senthil, Y. Zhang, F. Wang, L. Ju, *Science* **2022**, *375*, 1295.
[40] S. M. Gilbert, T. Pham, M. Dogan, S. Oh, B. Shevitski, G. Schumm, S. Liu, P. Ercius, S. Aloni, M. L. Cohen, *2D Mater.* **2019**, *5*, 021006.
[41] S. B. Song, S. Yoon, S. Y. Kim, S. Yang, S. Y. Seo, S. Cha, H. W. Jeong, K. Watanabe, T. Taniguchi, G. H. Lee, J. S. Kim, M. H. Jo, J. Kim, *Nat. Commun.* **2021**, *12*, 7134.
[42] N. Ubrig, E. Ponomarev, J. Zultak, D. Domaretskiy, V. Zólyomi, D. Terry, J. Howarth, I. Gutiérrez-Lezama, A. Zhukov, Z. R. Kudrynskyi, *Nat. Mater.* **2020**, *19*, 299.
[43] Q. Shi, E.-M. Shih, D. Rhodes, B. Kim, K. Barmak, K. Watanabe, T. Taniguchi, Z. Papić, D. A. Abanin, J. Hone, C. R. Dean, *Nat. Nanotechnol.* **2022**, *17*, 577.
[44] T. Li, S. Jiang, N. Sivadas, Z. Wang, Y. Xu, D. Weber, J. E. Goldberger, K. Watanabe, T. Taniguchi, C. J. Fennie, K. F. Mak, J. Shan, *Nat. Mater.* **2019**, *18*, 1303.
[45] T. Song, Z. Fei, M. Yankowitz, Z. Lin, Q. Jiang, K. Hwangbo, Q. Zhang, B. Sun, T. Taniguchi, K. Watanabe, M. A. McGuire, D. Graf, T. Cao, J.-H. Chu, D. H. Cobden, C. R. Dean, D. Xiao, X. Xu, *Nat. Mater.* **2019**, *18*, 1298.
[46] N. Sivadas, S. Okamoto, X. Xu, C. J. Fennie, D. Xiao, *Nano Lett.* **2018**, *18*, 7658.
[47] W. Chen, Z. Sun, Z. Wang, L. Gu, X. Xu, S. Wu, C. Gao, *Science* **2019**, *366*, 983.
[48] K. Yasuda, X. Wang, K. Watanabe, T. Taniguchi, P. Jarillo-Herrero, *Science* **2021**, *372*, 1458.
[49] M. V. Stern, Y. Waschitz, W. Cao, I. Nevo, K. Watanabe, T. Taniguchi, E. Sela, M. Urbakh, O. Hod, M. B. Shalom, *Science* **2021**, *372*, 1462.
[50] H. Hallil, W. Cai, K. Zhang, P. Yu, S. Liu, R. Xu, C. Zhu, Q. Xiong, Z. Liu, Q. Zhang, *Adv. Electron. Mater.* **2022**, http://doi.org/10.1002/aelm.202101131.
[51] J. Liu, S. T. Pantelides, *Phys. Rev. Lett.* **2018**, *120*, 207602.
[52] C.-J. Kim, L. Brown, M. W. Graham, R. Hovden, R. W. Havener, P. L. McEuen, D. A. Muller, J. Park, *Nano Lett.* **2013**, *13*, 5660.
[53] M. Zhao, Z. Ye, R. Suzuki, Y. Ye, H. Zhu, J. Xiao, Y. Wang, Y. Iwasa, X. Zhang, *Light: Sci. Appl.* **2016**, *5*, e16131.
[54] D. Xiao, W. Yao, Q. Niu, *Phys. Rev. Lett.* **2007**, *99*, 236809.
[55] L. Du, T. Hasan, A. Castellanos-Gomez, G.-B. Liu, Y. Yao, C. N. Lau, Z. Sun, *Nat. Rev. Phys.* **2021**, *3*, 193.
[56] Y. Liu, J. Xiao, J. Koo, B. Yan, *Nat. Mater.* **2021**, *20*, 638.
[57] C.-J. Kim, A. Sánchez-Castillo, Z. Ziegler, Y. Ogawa, C. Noguez, J. Park, *Nat. Nanotechnol.* **2016**, *11*, 520.
[58] Y. Gao, Y. Zhang, D. Xiao, *Phys. Rev. Lett.* **2020**, *124*, 077401.
[59] Y. Kim, H. Yun, S. G. Nam, M. Son, D. S. Lee, D. C. Kim, S. Seo, H. C. Choi, H. J. Lee, S. W. Lee, J. S. Kim, *Phys. Rev. Lett.* **2013**, *110*, 09660.
[60] S. Hong, C.-S. Lee, M.-H. Lee, Y. Lee, K. Y. Ma, G. Kim, S. I. Yoon, K. Ihm, K.-J. Kim, T. J. Shin, S. W. Kim, E. Jeon, H. Jeon, J.-Y. Kim, H.-I. Lee, Z. Lee, A. Antidormi, S. Roche, M. Chhowalla, H.-J. Shin, H. S. Shin, *Nature* **2020**, *582*, 511.
[61] A. P. Sutton, R. W. Balluffi, *Interfaces in Crystalline Materials*, Clarendon Press, Oxford **1995**.
[62] D. Hull, D. J. Bacon, *Introduction of Dislocation Theory*, Butterworth-Heinemann, Oxford **2001**.
[63] Z. Zhang, X. Zou, V. H. Crespi, B. I. Yakobson, *ACS Nano* **2013**, *7*, 10475.
[64] M. Phillips, E. J. Mele, *Phys. Rev. B* **2017**, *96*, 041403(R).

[65] N. Gao, Y. Guo, S. Zhou, Y. Bai, J. Zhao, *J. Phys. Chem. C* **2017**, *121*, 12261.
[66] H. J. Park, J. Cha, M. Choi, J. H. Kim, R. Y. Tay, E. H. T. Teo, N. Park, S. Hong, Z. Lee, *Sci. Adv.* **2020**, *6*, eaay4958.
[67] Y. C. Lin, T. Björkman, H. P. Komsa, P. Y. Teng, C. H. Yeh, F. S. Huang, K. H. Lin, J. Jadczak, Y. S. Huang, P. W. Chiu, A. V. Krasheninnikov, K. Suenaga, *Nat. Commun.* **2015**, *6*, 6736.
[68] X. Zou, B. I. Yakobson, *Small* **2015**, *11*, 4503.
[69] M. Gibertini, N. Marzari, *Nano Lett.* **2015**, *15*, 6229.
[70] S. Zhang, B. Huang, Y. Dai, W. Wei, *Comput. Mater. Sci.* **2022**, *203*, 111115.
[71] O. Lehtinen, H. P. Komsa, A. Pulkin, M. B. Whitwick, M. W. Chen, T. Lehnert, M. J. Mohn, O. V. Yazyev, A. Kis, U. Kaiser, A. V. Krasheninnikov, *ACS Nano* **2015**, *9*, 3274.
[72] W. Zhou, X. Zou, S. Najmaei, Z. Liu, Y. Shi, J. Kong, J. Lou, P. M. Ajayan, B. I. Yakobson, J. C. Idrobo, *Nano Lett.* **2013**, *13*, 2615.
[73] J. Lahiri, Y. Lin, P. Bozkurt, I. I. Oleynik, M. Batzill, *Nat. Nanotechnol.* **2010**, *5*, 326.
[74] K.-C. Kim, J. Lee, B. K. Kim, W. Y. Choi, H. J. Chang, S. O. Won, B. Kwon, S. K. Kim, D.-B. Hyun, H. J. Kim, H. C. Koo, J.-H. Choi, D.-I. Kim, J.-S. Kim, S.-H. Baek, *Nat. Commun.* **2016**, *7*, 12449.
[75] S. Barja, S. Wickenburg, Z.-F. Liu, Y. Zhang, H. Ryu, M. M. Ugeda, Z. Hussain, Z.-X. Shen, S.-K. Mo, E. Wong, M. B. Salmeron, F. Wang, M. F. Crommie, D. F. Ogletree, J. B. Neaton, A. Weber-Bargioni, *Nat. Phys.* **2016**, *12*, 751.
[76] S. Krishnamurthi, G. Brocks, *Phys. Rev. B* **2020**, *102*, 161106.
[77] Y. Ma, H. C. Diaz, J. Avila, C. Chen, V. Kalappattil, R. Das, M.-H. Phan, T. Cˇadež, J. M. P. Carmelo, M. C. Asensio, M. Batzill, *Nat. Commun.* **2017**, *8*, 14231.
[78] C. T. Toh, H. Zhang, J. Lin, A. S. Mayorov, Y. P. Wang, C. M. Orofeo, D. B. Ferry, H. Andersen, N. Kakenov, Z. Guo, I. H. Abidi, H. Sims, K. Suenaga, S. T. Pantelides, B. Özyilmaz, *Nature* **2020**, *577*, 199.
[79] B. Feng, X. Zhuang, *Faraday Discuss.* **2021**, *227*, 80.
[80] S. M. Kim, A. Hsu, M. H. Park, S. H. Chae, S. J. Yun, J. S. Lee, D.-H. Cho, W. Fang, C. Lee, T. Palacios, M. Dresselhaus, K. K. Kim, Y. H. Lee, J. Kong, *Nat. Commun.* **2015**, *6*, 8662.
[81] L. Sun, Z. Wang, Y. Wang, L. Zhao, Y. Li, B. Chen, S. Huang, S. Zhang, W. Wang, D. Pei, H. Fang, S. Zhong, H. Liu, J. Zhang, L. Tong, Y. Chen, Z. Li, M. H. Rümmeli, K. S. Novoselov, H. Peng, L. Lin, Z. Liu, *Nat. Commun.* **2021**, *12*, 2391.
[82] L. Brown, R. Hovden, P. Huang, M. Wojcik, D. A. Muller, J. Park, *Nano Lett.* **2012**, *12*, 1609.
[83] F. Meng, S. A. Morin, A. Forticaux, S. Jin, *Acc. Chem. Res.* **2013**, *46*, 1616.
[84] L. Chen, B. Liu, A. N. Abbas, Y. Ma, X. Fang, Y. Liu, C. Zhou, *ACS Nano* **2014**, *8*, 11543.
[85] L. Zhang, K. Liu, A. B. Wong, J. Kim, X. Hong, C. Liu, T. Cao, S. G. Louie, F. Wang, P. Yang, *Nano Lett.* **2014**, *14*, 6418.
[86] M. J. Shearer, L. Samad, Y. Zhang, Y. Zhao, A. Puretzky, K. W. Eliceiri, J. C. Wright, R. J. Hamers, S. Jin, *J. Am. Chem. Soc.* **2017**, *139*, 3496.
[87] P. Sutter, S. Wimer, E. Sutter, *Nature* **2019**, *570*, 354.
[88] Y. Liu, J. Wang, S. Kim, H. Sun, F. Yang, Z. Fang, N. Tamura, R. Zhang, X. Song, J. Wen, B. Z. Xu, M. Wang, S. Lin, Q. Yu, K. B. Tom, Y. Deng, J. Turner, E. Chan, D. Jin, R. O. Ritchie, A. M. Minor, D. C. Chrzan, M. C. Scott, J. Yao, *Nature* **2019**, *570*, 358.
[89] Y. Zhao, C. Zhang, D. D. Kohler, J. M. Scheeler, J. C. Wright, P. M. Voyles, S. Jin, *Science* **2020**, *370*, 442.
[90] F. Laves, Y. Baskin, *Z. Kristallogr.* **1956**, *107*, 337.
[91] Y. Yang, Y.-C. Zou, C. R. Woods, Y. Shi, J. Yin, S. Xu, S. Ozdemir, T. Taniguchi, K. Watanabe, A. K. Geim, K. S. Novoselov, S. J. Haigh, A. Mishchenko, *Nano Lett.* **2019**, *19*, 8526.
[92] J. P. Nery, M. Calandra, F. Mauri, *Nano Lett.* **2020**, *20*, 5017.
[93] Z. Gao, S. Wang, J. Berry, Q. Zhang, J. Gebhardt, W. M. Parkin, J. Avila, H. Yi, C. Chen, S. Hurtado-Parra, M. Drndic, A. M. Rappe, D. J. Srolovitz, J. M. Kikkawa, Z. Luo, M. C. Asensio, F. Wang, A. T. C. Johnson, *Nat. Commun.* **2020**, *11*, 546.
[94] H. Li, M. I. B. Utama, S. Wang, W. Zhao, S. Zhao, X. Xiao, Y. Jiang, L. Jiang, T. Taniguchi, K. Watanabe, A. Weber-Bargioni, A. Zettl, F. Wang, *Nano Lett.* **2020**, *20*, 3106.
[95] V. L. Nguyen, D. L. Duong, S. H. Lee, J. Avila, G. Han, Y.-M. Kim, M. C. Asensio, S.-Y. Jeong, Y. H. Lee, *Nat. Nanotechnol.* **2020**, *15*, 861.
[96] J. S. Alden, A. W. Tsen, P. Y. Huang, R. Hovden, L. Brown, J. Park, D. A. Muller, P. L. McEuen, *Proc. Natl. Acad. Sci. USA* **2013**, *110*, 11256.
[97] K. Kim, M. Yankowitz, B. Fallahazad, S. Kang, H. C. P. Movva, S. Huang, S. Larentis, C. M. Corbet, T. Taniguchi, K. Watanabe, S. K. Banerjee, B. J. LeRoy, E. Tutuc, *Nano Lett.* **2016**, *16*, 1989.
[98] Y. Cao, J. Y. Luo, V. Fatemi, S. Fang, J. D. Sanchez-Yamagishi, K. Watanabe, T. Taniguchi, E. Kaxiras, P. Jarillo-Herrero, *Phys. Rev. Lett.* **2016**, *117*, 116804.
[99] C. R. Dean, A. F. Young, I. Meric, C. Lee, L. Wang, S. Sorgenfrei, K. Watanabe, T. Taniguchi, P. Kim, K. L. Shepard, J. Hone, *Nat. Nanotechnol.* **2010**, *5*, 722.
[100] F. Liu, W. Wu, Y. Bai, S. H. Chae, Q. Li, J. Wang, J. Hone, X.-Y. Zhu, *Science* **2020**, *367*, 903.
[101] J.-Y. Moon, M. Kim, S.-I. Kim, S. Xu, J.-H. Choi, D. Whang, K. Watanabe, T. Taniguchi, D. S. Park, J. Seo, S. H. Cho, S.-K. Son, J.-H. Lee, *Sci. Adv.* **2020**, *6*, eabc6601.
[102] T.-A. Chen, C.-P. Chuu, C.-C. Tseng, C.-K. Wen, H. P. Wong, S. Pan, R. Li, T.-A. Chao, W.-C. Chueh, Y. Zhang, Q. Fu, B. I. Yakobson, W.-H. Chang, L.-J. Li, *Nature* **2020**, *579*, 219.
[103] T. Li, W. Guo, L. Ma, W. Li, Z. Yu, Z. Han, S. Gao, L. Liu, D. Fan, Z. Wang, Y. Yang, W. Lin, Z. Luo, X. Chen, N. Dai, X. Tu, D. Pan, Y. Yao, P. Wang, Y. Nie, J. Wang, Y. Shi, X. Wang, *Nat. Nanotechnol.* **2021**, *16*, 1201.
[104] J. Wang, X. Xu, T. Cheng, L. Gu, R. Qiao, Z. Liang, D. Ding, H. Hong, P. Zheng, Z. Zhang, Z. Zhang, S. Zhang, G. Cui, C. Chang, C. Huang, J. Qi, J. Liang, C. Liu, Y. Zuo, G. Xue, X. Fang, J. Tian, M. Wu, Y. Guo, Z. Yao, Q. Jiao, L. Liu, P. Gao, Q. Li, R. Yang, et al., *Nat. Nanotechnol.* **2022**, *17*, 33.
[105] S.-J. Yang, S. Choi, F. O. O. Ngome, K.-J. Kim, S.-Y. Choi, C.-J. Kim, *Nano Lett.* **2019**, *19*, 3590.
[106] S.-J. Yang, J.-H. Jung, E. Lee, E. Han, M.-Y. Choi, D. Jung, S. Choi, J.-H. Park, D. Oh, S. Noh, K.-J. Kim, P. Y. Huang, C.-C. Hwang, C.-J. Kim, *Nano Lett.* **2022**, *22*, 1518.
[107] Y.-C. Lin, C.-C. Lu, C.-H. Yeh, C. Jin, K. Suenaga, P.-W. Chiu, *Nano Lett.* **2012**, *12*, 414.
[108] F. Xia, H. Wang, J. C. M. Hwang, A. H. C. Neto, L. Yang, *Nat. Rev. Phys.* **2019**, *1*, 306.
[109] D. M. Kennes, L. Xian, M. Claassen, A. Rubio, *Nat. Commun.* **2020**, *11*, 1124.
[110] A. J. Mannix, A. Ye, S. H. Sung, A. Ray, F. Mujid, C. Park, M. Lee, J.-H. Kang, R. Shreiner, A. A. High, D. A. Muller, R. Hovden, J. Park, *Nat. Nanotechnol.* **2022**, *17*, 361.
[111] Y. Wang, V. H. Crespi, *Nano Lett.* **2017**, *17*, 5297.
[112] H. Yu, N. Gupta, Z. Hu, K. Wang, B. R. Srijanto, K. Xiao, D. B. Geohegan, B. I. Yakobson, *ACS Nano* **2017**, *11*, 8612.
[113] A. W. Tsen, L. Brown, M. P. Levendorf, F. Ghahari, P. Y. Huang, R. W. Havener, C. S. Ruiz-vargas, D. A. Muller, P. Kim, J. Park, *Science* **2012**, *336*, 1143.
[114] J. Dong, L. Zhang, X. Dai, F. Ding, *Nat. Commun.* **2020**, *11*, 5862.
[115] Q. Wang, N. Li, J. Tang, J. Zhu, Q. Zhang, Q. Jia, Y. Lu, Z. Wei, H. Yu, Y. Zhao, Y. Guo, L. Gu, G. Sun, W. Yang, R. Yang, D. Shi, G. Zhang, *Nano Lett.* **2020**, *20*, 7193.
[116] G. Jin, C.-S. Lee, O. F. N. Okello, S.-H. Lee, M. Y. Park, S. Cha, S.-Y. Seo, G. Moon, S. Y. Min, D.-H. Yang, C. Han, H. Ahn, J. Lee, H. Choi, J. Kim, S.-Y. Choi, M.-H. Jo, *Nat. Nanotechnol.* **2021**, *16*, 1092.

[117] T. Chowdhury, J. Kim, E. C. Sadler, C. Li, S. W. Lee, K. Jo, W. Xu, D. H. Gracias, N. V. Drichko, D. Jariwala, T. H. Brintlinger, T. Mueller, H. Park, T. J. Kempa, *Nat. Nanotechnol.* **2020**, *15*, 29.
[118] Y. Li, H. Liu, Z. Chang, H. Li, S. Wang, L. Lin, H. Peng, Y. Wei, L. Sun, Z. Liu, *Adv. Mater.* **2022**, https://doi.org/10.1002/adma.202201188.
[119] X. Zhou, Z. Zhang, W. Guo, *Nano Lett.* **2020**, *20*, 4136.
[120] Q. Li, X. Zou, M. Liu, J. Sun, Y. Gao, Y. Qi, X. Zhou, B. I. Yakobson, Y. Zhang, Z. Liu, *Nano Lett.* **2015**, *15*, 5804.
[121] H. P. Komsa, A. V. Krasheninnikov, *Adv. Electron. Mater.* **2017**, *3*, 1600468.
[122] X. Ren, X. Wang, C. Jin, *Nano Lett.* **2019**, *19*, 8581.
[123] A. M. Van Der Zande, P. Y. Huang, D. A. Chenet, T. C. Berkelbach, Y. You, G. H. Lee, T. F. Heinz, D. R. Reichman, D. A. Muller, J. C. Hone, *Nat. Mater.* **2013**, *12*, 554.
[124] K. V. Bets, V. I. Artyukhov, B. I. Yakobson, *ACS Nano* **2021**, *15*, 4893.
[125] M.-Y. Choi, C.-W. Choi, S.-J. Yang, H. Lee, S. Choi, J.-H. Park, J. Heo, S.-Y. Choi, C.-J. Kim, *ACS Appl. Nano Mater.* **2022**, *5*, 4336.
[126] X. Zhao, P. Song, C. Wang, A. C. Riis-Jensen, W. Fu, Y. Deng, D. Wan, L. Kang, S. Ning, J. Dan, T. Venkatesan, Z. Liu, W. Zhou, K. S. Thygesen, X. Luo, S. J. Pennycook, K. P. Loh, *Nature* **2020**, *581*, 171.
[127] X. Zhao, D. Fu, Z. Ding, Y. Y. Zhang, D. Wan, S. J. R. Tan, Z. Chen, K. Leng, J. Dan, W. Fu, D. Geng, P. Song, Y. Du, T. Venkatesan, S. T. Pantelides, S. J. Pennycook, W. Zhou, K. P. Loh, *Nano Lett.* **2018**, *18*, 482.
[128] X. Zou, M. Liu, Z. Shi, B. I. Yakobson, *Nano Lett.* **2015**, *15*, 3495.
[129] X. Sang, X. Li, W. Zhao, J. Dong, C. M. Rouleau, D. B. Geohegan, F. Ding, K. Xiao, R. R. Unocic, *Nat. Commun.* **2018**, *9*, 2051.
[130] V. H. Nguyen, S. Dechamps, P. Dollfus, J.-C. Charlier, *Phys. Rev. Lett.* **2016**, *117*, 247702.
[131] J. Dong, D. Geng, F. Liu, F. Ding, *Angew. Chem., Int. Ed.* **2019**, *58*, 7723.
[132] V. K. Sangwan, D. Jariwala, I. S. Kim, K.-S. Chen, T. J. Marks, L. J. Lauhon, M. C. Hersam, *Nat. Nanotechnol.* **2015**, *10*, 403.
[133] T. H. Ly, D. J. Perello, J. Zhao, Q. Deng, H. Kim, G. H. Han, S. H. Chae, H. Y. Jeong, Y. H. Lee, *Nat. Commun.* **2016**, *7*, 10426.
[134] J. Wang, X. Cai, R. Shi, Z. Wu, W. Wang, G. Long, Y. Tang, N. Cai, W. Ouyang, P. Geng, B. N. Chandrashekar, A. Amini, N. Wang, C. Cheng, *ACS Nano* **2018**, *12*, 635.
[135] X. Wang, B. Wang, Q. Zhang, Y. Sun, E. Wang, H. Luo, Y. Wu, L. Gu, H. Li, K. Liu, *Adv. Mater.* **2021**, *33*, 2102435.
[136] C. Murray, C. Van Efferen, W. Jolie, J. A. Fischer, J. Hall, A. Rosch, A. V. Krasheninnikov, H. P. Komsa, T. Michely, *ACS Nano* **2020**, *14*, 9176.
[137] N. Kim, S. Choi, S.-J. Yang, J. Park, J.-H. Park, N. N. Nguyen, K. Park, S. Ryu, K. Cho, C.-J. Kim, *ACS Appl. Mater. Interfaces* **2021**, *13*, 28593.
[138] A. J. Way, R. M. Jacobberger, M. S. Arnold, *Nano Lett.* **2018**, *18*, 898.
[139] X. Z. Xu, Z. H. Zhang, L. Qiu, J. N. Zhuang, L. Zhang, H. Wang, C. N. Liao, H. D. Song, R. X. Qiao, P. Gao, Z. H. Hu, L. Liao, Z. M. Liao, D. P. Yu, E. G. Wang, F. Ding, H. L. Peng, K. Liu, *Nat. Nanotechnol.* **2016**, *11*, 930.
[140] C. Liu, X. Z. Xu, L. Qiu, M. H. Wu, R. X. Qiao, L. Wang, J. H. Wang, J. J. Niu, J. Liang, X. Zhou, Z. H. Zhang, M. Peng, P. Gao, W. L. Wang, X. D. Bai, D. Ma, Y. Jiang, X. S. Wu, D. P. Yu, E. G. Wang, J. Xiong, F. Ding, K. Liu, *Nat. Chem.* **2019**, *11*, 730.
[141] T. R. Wu, X. F. Zhang, Q. H. Yuan, J. C. Xue, G. Y. Lu, Z. H. Liu, H. S. Wang, H. M. Wang, F. Ding, Q. K. Yu, X. M. Xie, M. H. Jiang, *Nat. Mater.* **2016**, *15*, 43.
[142] D. R. Hickey, N. Nayir, M. Chubarov, T. H. Choudhury, S. Bachu, L. Miao, Y. Wang, C. Qian, V. H. Crespi, J. M. Redwing, A. C. T. van Duin, N. Alem, *Nano Lett.* **2021**, *15*, 6487.
[143] L. Banszerus, M. Schmitz, S. Engels, J. Dauber, M. Oellers, F. Haupt, K. Watanabe, T. Taniguchi, B. Beschoten, C. Stampfer, *Sci. Adv.* **2015**, *1*, e1500222.
[144] A. V. Stier, N. P. Wilson, G. Clark, X. Xu, S. A. Crooker, *Nano Lett.* **2016**, *16*, 7054.
[145] M. Van der Donck, F. M. Peeters, *Phys. Rev. B* **2018**, *98*, 115104.
[146] J. V. Lauritsen, J. Kibsgaard, S. Helveg, H. Topsøe, B. S. Clausen, E. Lægsgaard, F. Besenbacher, *Nat. Nanotechnol.* **2007**, *2*, 53.
[147] M. P. Levendorf, C.-J. Kim, L. Brown, P. Y. Huang, R. W. Havener, D. A. Muller, J. Park, *Nature* **2012**, *488*, 627.
[148] S. J. Ahn, P. Moon, T.-H. Kim, H.-W. Kim, H.-C. Shin, E. H. Kim, H. W. Cha, S.-J. Kahng, P. Kim, M. Koshino, Y.-W. Son, C.-W. Yang, J. R. Ahn, *Science* **2018**, *361*, 782.
[149] E. J. Mele, *Phys. Rev. B* **2010**, *81*, 161405.
[150] A. Weston, E. G. Castanon, V. Enaldiev, F. Ferreira, S. Bhattacharjee, S. Xu, H. Corte-León, Z. Wu, N. Clark, A. Summerfield, T. Hashimoto, Y. Gao, W. Wang, M. Hamer, H. Read, L. Fumagalli, A. V. Kretinin, S. J. Haigh, O. Kazakova, A. K. Geim, V. I. Fal'ko, R. Gorbachev, *Nat. Nanotechnol.* **2022**, *17*, 390.
[151] L. Wang, E.-M. Shih, A. Ghiotto, L. Xian, D. A. Rhodes, C. Tan, M. Claassen, D. M. Kennes, Y. Bai, B. Kim, K. Watanabe, T. Taniguchi, X. Zhu, J. Hone, A. Rubio, A. Pasupathy, C. R. Dean, *Nat. Mater.* **2020**, *19*, 861.
[152] C. R. Woods, P. Ares, H. Nevison-Andrews, M. J. Holwill, R. Fabregas, F. Guinea, A. K. Geim, K. S. Novoselov, N. R. Walet, L. Fumagalli, *Nat. Commun.* **2021**, *12*, 347.
[153] H. Y. Lee, M. M. Al Ezzi, N. Raghuvanshi, J. Y. Chung, K. Watanabe, T. Taniguchi, S. Garaj, S. Adam, S. Gradečak, *Nano Lett.* **2021**, *21*, 2832.
[154] L. Xian, A. Fischer, M. Claassen, J. Zhang, A. Rubio, D. M. Kennes, *Nano Lett.* **2021**, *21*, 7519.
[155] B. Yang, H. Xu, J. Lu, K. P. Loh, *J. Am. Chem. Soc.* **2014**, *136*, 12041.
[156] Y. Liu, X. Zou, B. I. Yakobson, *ACS Nano* **2012**, *6*, 7053.
[157] Y. L. Huang, Z. Ding, W. Zhang, Y.-H. Chang, Y. Shi, L.-J. Li, Z. Song, Y. J. Zheng, D. Chi, S. Y. Quek, A. T. S. Wee, *Nano Lett.* **2016**, *16*, 3682.
[158] D. Wang, H. Yu, L. Tao, W. Xiao, P. Fan, T. Zhang, M. Liao, W. Guo, D. Shi, S. Du, G. Zhang, H. Gao, *Nano Res.* **2018**, *11*, 6102.
[159] A. Pulkin, O. V. Yazyev, *Phys. Rev. B* **2016**, *93*, 041419.
[160] S. Masubuchi, M. Morimoto, S. Morikawa, M. Onodera, Y. Asakawa, K. Watanabe, T. Taniguchi, T. Machida, *Nat. Commun.* **2018**, *9*, 1413.
[161] M. Liao, Z. Wei, L. Du, Q. Wang, J. Tang, H. Yu, F. Wu, J. Zhao, X. Xu, B. Han, K. Liu, P. Gao, T. Polcar, Z. Sun, D. Shi, R. Yang, G. Zhang, *Nat. Commun.* **2020**, *11*, 2153.
[162] H. Chen, X.-L. Zhang, Y.-Y. Zhang, D. Wang, D.-L. Bao, Y. Que, W. Xiao, S. Du, M. Ouyang, S. T. Pantelides, H.-J. Gao, *Science* **2019**, *365*, 1036.
[163] B. Wang, M. Huang, N. Y. Kim, B. V. Cunning, Y. Huang, D. Qu, X. Chen, S. Jin, M. Biswal, X. Zhang, S. H. Lee, H. Lim, W. J. Yoo, Z. Lee, R. S. Ruoff, *Nano Lett.* **2017**, *17*, 1467.

Seong-Jun Yang is currently a Ph.D. candidate in the Department of Chemical Engineering at Pohang University of Science and Technology (POSTECH). He obtained his B.S. degree from Ajou University in 2017. His current research interests focus on growth and assembly of graphene and hexagonal boron nitride for advanced electronic devices.

Min-Yeong Choi is currently a Ph.D. candidate in the Department of Chemical Engineering at POSTECH. He obtained his B.S. degree from Chungnam National University in 2020. His current research interests focus on emergent properties of various grain boundaries in 2D materials.

Cheol-Joo Kim is an assistant professor in the Department of Chemical Engineering at POSTECH. He received his Ph.D. degree from POSTECH in 2011. His current research interests focus on the growth and structural engineering of two-dimensional materials for various nano-devices with advanced functionalities.